

1 **Upscaling instantaneous to daily evapotranspiration using**
2 **modelled daily shortwave radiation for remote sensing**
3 **applications: an Artificial Neural Network approach**

4 Loise Wandera^{1,2}, Kaniska Mallick¹, Gerard Kiely³, Olivier Roupsard⁴, Matthias Peichl⁵,
5 Vincenzo Magliulo⁶

6 ¹Remote Sensing and Ecohydrological Modeling, Dept. ERIN, Luxembourg Institute of Science and
7 Technology, Belvaux, Luxembourg

8 ²Water Resources, Dept. ITC, University of Twente, Enschede, Netherlands

9 ³Hydrology, Micrometeorology & Climate Investigations, HYDROMET Research Group, University College
10 Cork, Ireland

11 ⁴CIRAD, UMR Ecology and Soils, Montpellier, France

12 ⁵Forest Landscape Biogeochemistry, Dept. Swedish University of Agricultural Sciences Umeå, Sweden

13 ⁶Consiglio Nazionale delle Ricerche, ISAFOM, Ercolano, Napoli, Italy

14

15

16 Correspondence to: Kaniska Mallick (Phone: +352 275888425; email:
17 kaniska.mallick@gmail.com); Loise Wandera (email: loise.wandera@list.lu);

18

19

20

21

22

23

24

1 **Abstract**

2 Upscaling instantaneous evapotranspiration retrieved at any specific time-of-day (ET_i) to daily
3 evapotranspiration (ET_d) is a key challenge in mapping regional ET using polar orbiting
4 sensors. Various studies have unanimously cited the short wave incoming radiation (R_S) to be
5 the most robust reference variable explaining the ratio between ET_d and ET_i . This study aims
6 to contribute in ET_i upscaling for global studies using the ratio between daily and
7 instantaneous incoming short wave radiation (R_{Sd}/R_{Si}) as a factor for converting ET_i to ET_d .

8 This paper proposes an artificial neural network (ANN) machine learning algorithm first to
9 predict R_{Sd} from R_{Si} followed by using the R_{Sd}/R_{Si} ratio to convert ET_i to ET_d across different
10 terrestrial ecosystem. Using R_{Si} and R_{Sd} observations from multiple sub-networks of
11 FLUXNET database spread across different climates and biomes (to represent inputs that
12 would typically be obtainable from remote sensors during the overpass time) in conjunction
13 with some astronomical variables (e.g., solar zenith angle, day length, exoatmospheric
14 shortwave radiation etc.), we developed ANN model for reproducing R_{Sd} and further used it to
15 upscale ET_i to ET_d . The efficiency of the ANN is evaluated for different morning and
16 afternoon time-of-day, under varying sky conditions, and also at different geographic
17 locations. R_S -based upscaled ET_d produced a significant linear relation ($R^2 = 0.65$ to 0.69),
18 low bias (-0.31 to -0.56 MJ m⁻² d⁻¹) (appx. 4%), and good agreement (RMSE 1.55 to 1.86 MJ
19 m⁻² d⁻¹) (appx. 10%) with the observed ET_d , although a systematic overestimation of ET_d was
20 also noted under persistent cloudy sky conditions. Inclusion of soil moisture and rainfall
21 information in ANN training reduced the systematic overestimation tendency in
22 predominantly overcast days. An intercomparison with existing upscaling method at daily, 8-
23 day, monthly, and yearly temporal resolution revealed a robust performance of the ANN
24 driven R_S -based ET_i upscaling method and was found to produce lowest RMSE under cloudy
25 conditions. Sensitivity analysis revealed variable sensitivity of the method to biome selection
26 and high ET_d prediction errors in forest ecosystems are primarily associated with greater
27 rainfall and clouds. The overall methodology appears to be promising and has substantial
28 potential for upscaling ET_i to ET_d for field and regional scale evapotranspiration mapping
29 studies using polar orbiting satellites.

1 *Key Words:* Evapotranspiration, upscaling, artificial neural networks, short wave radiation,
2 rainfall, soil moisture, FLUXNET

3 **1 Introduction**

4 Satellite-based mapping and monitoring of daily regional evapotranspiration (*ET* hereafter)
5 (or latent heat flux, λE) is considered as a key scientific concern for multitudes of applications
6 including drought monitoring, water rights management, ecosystem water use efficiency
7 assessment, distributed hydrological modelling, climate change studies, and numerical
8 weather prediction (Anderson et al., 2015; Senay et al., 2015; Sepulcre-Canto et al., 2014). *ET*
9 variability during the course of a day is influenced by changes in the radiative energy being
10 received at the surface (Brutsaert & Sugita, 1992; Crago, 1996; Parlange & Katul, 1992), due
11 to soil moisture variability particularly in the water deficit landscapes, and also due to the
12 stomatal regulation by vegetation.

13 One of the fundamental challenges in regional *ET* modelling using polar orbiting satellites
14 involves the upscaling of instantaneous *ET* retrieved at any specific time-of-day (ET_i
15 hereafter) to daily *ET* (ET_d hereafter). For example, ET_i retrieved from LANDSAT, ASTER
16 and MODIS sensors typically represent ET_i at a single snapshot of 1000, 1030 and 1330 hrs
17 local time, which needs to be upscaled to daily timescale for making this information usable
18 to hydrologists and water managers (Cammalleri et al., 2014; Colaizzi et al., 2006; Ryu et al.,
19 2012; Tang et al., 2013).

20 In order to accommodate the temporal scaling challenges encountered by remote sensing
21 based *ET* models, techniques have been proposed and applied by various researchers to
22 upscale ET_i to ET_d . These include: (1) the constant evaporative fraction (*EF*) approach which
23 assumes a constant ratio between λE and net available energy ($\phi = R_n - G$, R_n is the net
24 radiation and G is the ground heat flux) during daytime [$EF = \lambda E / (R_n - G)$] (Gentine et al.,
25 2007; Shuttleworth et al., 1989), (2) constant reference evaporative fractions (EF_r) method
26 where the ratio of ET_i between a reference crop (typically grass measuring a height of 0.12 m
27 in an environment that is not water limited) and an actual surface is assumed to be constant
28 during daytime, allowing ET_d to be estimated from the daily EF_r (Allen et al., 1998; Tang et
29 al., 2013), (3) constant global shortwave radiation method (R_S) where R_S is the reference
30 variable at the land surface and it is assumed that the ratio of daily to instantaneous shortwave

1 radiation (R_{Sd} and R_{Si}) values (i.e., R_{Sd}/R_{Si}) determines ET_d to ET_i ratio (Jackson et al., 1983;
2 Cammalleri et al., 2014), and (4) constant extra-terrestrial radiation method where the exo-
3 atmospheric shortwave radiation ($R_S TOA$) is the reference variable and the ratio of
4 instantaneous to daily $R_S TOA$ ($R_{Si} TOA$ and $R_{Sd} TOA$) is assumed to determine the ratio of ET_d
5 to ET_i (Ryu et al., 2012; Van Niel et al., 2012). These methods have been reviewed and
6 compared in different studies with the view of identifying the most robust ET_i to ET_d
7 upscaling approach based on different data sets, time integrals and varying sky conditions
8 (Cammalleri et al., 2014; Ryu et al., 2012; Tang et al, 2013, 2015; Van Niel et al., 2012; Xu et
9 al., 2015).

10 Based on the previous studies, we find that the $R_S TOA$ approach performed consistently good
11 at lower temporal resolution namely eight-day to monthly scales (Ryu et al., 2012; Van Niel
12 et al., 2012) as well as under clear-sky conditions (Cammalleri et al., 2014), whereas the R_S
13 approach was identified as the most preferred method for ET_i to ET_d conversion at a higher
14 temporal scale i.e. daily timescale in addition to under variable sky conditions (Cammalleri et
15 al., 2014; Chávez et al., 2008; Colaizzi, et al., 2006; Xu et al., 2015). Although the EF_r -based
16 method produced comparable ET_d estimates as the R_S -based method, however the dependence
17 of EF_r estimates on certain variables (e.g., daily net available energy; ϕ and wind speed) and
18 the difficulty to characterise them at the daily scale from single acquisition of polar orbiting
19 satellites (Tang et al., 2015) makes it a relatively less attractive method. Furthermore the EF -
20 based method appeared to consistently underestimate ET_d in all these studies.

21 The motivation of the current work is built on the conclusions of Colaizzi et al. (2006),
22 Chávez et al. (2008), Cammalleri et al. (2014), and Xu et al. (2015) that the ratio of the
23 instantaneous to daily R_S incident on land surface is the most robust reference variable
24 explaining the ratio between ET_d and ET_i among all the tested methods. This work aims to
25 contribute in ET_i upscaling by first developing a method for estimating R_{Sd} from any specific
26 time-of-day R_S information (R_{Si}) and further using R_{Sd}/R_{Si} ratio as a factor for converting ET_i
27 to ET_d . We develop an artificial neural network (ANN) machine learning algorithm
28 (McCulloch & Pitts, 1943) for estimating R_{Sd} . Although net radiation (R_N) is more closely
29 associated with ET , but R_S constitutes 80-85% of R_N (Mallick et al., 2015). Also from remote
30 sensing perspective, R_{Si} is relatively easily retrievable irrespective of the sky conditions
31 (Wang et al., 2015; Lopez and Batlles, 2014), and its relationship to R_{Sd} is primarily governed

1 by cloudiness (cloud fraction, cloud optical depth) and astronomical variables (e.g., solar
2 zenith angle, day length, $R_{S_{TOA}}$ etc.). Given the information of cloudiness is also obtainable
3 from remote sensing, we consider R_S to be a robust variable to explore ET_i upscaling.

4 Even though this study is intended for remote sensing application, we tested the method using
5 meteorological and surface energy balance flux measurements from eddy covariance (EC)
6 system at the FLUXNET (Baldocchi et al., 2001) sites mainly for the purpose of temporal
7 consistency. However, we evaluate the performance in consideration with overpass time of
8 polar orbiting satellites commonly used in operational ET mapping namely MODIS and
9 LANDSAT. By choosing to use data distributed over different ecosystems and climates
10 zones, we are faced with two problems : (1) changing cloud conditions across ecosystems, (2)
11 varying energy balance closure (EBC) requirements for the fluxes in different ecosystems
12 (Foken et al., 2006; Franssen et al., 2010; Mauder & Foken, 2006; Wilson et al., 2002).
13 Currently, information on cloudiness is obtainable from geostationary meteorological
14 satellites, at hourly to 3-hourly time steps e.g., from the Clouds and Earth's Radiant Energy
15 System (CERES), the International Satellite Cloud Climatology Project–Flux Data (ISCCP-
16 FD), and Global Energy and Water cycle Experiment Surface Radiation Budget (GEWEX-
17 SRB). The CERES algorithm uses cloud information from MODIS onboard both Terra and
18 Aqua platforms and combines it with information from geostationary satellites to accurately
19 capture the diurnal cycles of clouds. In this study, cloudiness is not included in the list of
20 variables used to estimate R_{S_d} due to inconsistency in spatial resolution of data to match with
21 the other predictive variables used. Including cloudiness holds a great potential in improving
22 the ANN R_{S_d} predications due to their direct relationship (Mallick et al., 2015). However, we
23 assess the performance of the ANN under cloudy sky conditions based on simple cloudiness
24 index computations as adopted from previous works (Baigorria et al., 2004). The EBC
25 problems have been reported to vary across landscapes due to management practices, climate,
26 seasons and plant functional type characteristics (Foken et al., 2006). In this study, in order to
27 test the robustness of the proposed method, we initially disregard the site specific EBC
28 problems and assume that the systematic bias of fluxes fall within the same range across
29 entire FLUXNET database used.

30 The objectives of the present study are: (1) using a ANN with Multilayer Perceptron (MLP)
31 architecture to predict R_{S_d} based on R_{S_i} satellite observations, (2) applying R_{S_d}/R_{S_i} ratio as a

1 scaling factor to upscale ET_i to ET_d under all sky conditions, and (3) comparing the
2 performance of proposed R_S -based ET_i upscaling method with $R_S TOA$ and EF -based ET_i
3 upscaling methods across a range of temporal scales, biomes and variable sky conditions.

4 **2 Methodology**

5 **2.1 Rationale**

6 The presented method of ET upscaling from any specific time-of-day to daytime average
7 evaporative fluxes is based on the assumption of self-preservation of incoming solar energy
8 (i.e., shortwave radiation) as proposed by Jackson et al. (1983).

$$9 \quad ET_d \approx ET_i \frac{R_{Sd}}{R_{Si}} \quad (1)$$

10 Where, ET_d is the daily average evapotranspiration in $W m^{-2}$, ET_i is the instantaneous
11 evapotranspiration at any instance during daytime in $W m^{-2}$, R_{Si} and R_{Sd} are the values of
12 shortwave radiation recorded at any instance and the daily average having units $W m^{-2}$. Daily
13 total ET_d and R_{Sd} is expressed in $MJ m^{-2} d^{-1}$ by using standard conversion from Watts to Mega
14 Joules. Following Jackson et al. (1983) and Cammalleri et al. (2014), we hypothesized that
15 the mean diurnal variation of ET for any particular day scales with the mean diurnal variation
16 of R_S . The justifications are: (a) R_S is the principal driver that controls sub-daily ET variability
17 unless there is substantial diurnal asymmetry in cloudiness or abrupt change in sub-daily soil
18 moisture between morning and afternoon. (b) Under thick cloudy conditions, ET scales with
19 R_S . Under clear sky conditions ET also scales with R_S and both are in phase if sufficient soil
20 moisture is available at the surface. (c) Phase difference between R_S and ET are commonly
21 found under soil moisture deficit conditions in clear-sky days. However, the magnitude of
22 clear-sky ET_i in water deficit conditions is also be very low, which will lead to substantially
23 low ET_i/R_{Si} ratio, and would unlikely to introduce any uncertainty in ET_i to ET_d upscaling in
24 the framework of eq. (1).

25 For any remote sensing studies using polar orbiting satellites, although the retrieval of ET_i and
26 R_{Si} has been standardised (Tang et al., 2015; Huang et al., 2012; Polo et al., 2008; Laine et al.,
27 1999), but, estimating R_{Sd} and ET_d from R_{Si} and ET_i are still challenging. Presently, upscaling
28 R_{Si} to R_{Sd} is primarily based on the clear sky assumption, i.e., for the entire daytime

1 integration period, the sky remains cloud-free (Bisht et al., 2005; Jackson et al., 1983).
2 However, the clear-sky assumption is not always appropriate for upscaling remote sensing
3 based R_{Si} and hence ET_i because the sky conditions during a specific time-of-day may be clear
4 whereas the other part of the day might be cloudy. Under such conditions, the clear-sky
5 assumption of ET_i upscaling will lead to substantial overestimation of ET_d in cloudy
6 conditions. Hence reliable estimates of all-sky (i.e., both clear and cloudy) R_{Sd} would greatly
7 improve the ET_d estimates in the framework of eq. (1). Given the unavailability of a definite
8 method to directly estimate all-sky R_{Sd} from R_{Si} information, here we proposed a simple
9 method to upscale R_{Si} to R_{Sd} using ANN. This method uses the observations of both R_{Sd} and
10 R_{Si} from all the available FLUXNET sites in conjunction with some ancillary variables to
11 build the ANN as described in section 2.2. A schematic diagram of the ANN method is given
12 in Fig. 1. The analysis is based on 24-hour period, meaning night time ET contribution is
13 implicitly considered. However, studies have already shown that the nighttime ET in semi-
14 arid and sub-humid regions contributes only 2 – 5% of the total season ET (Malek, 1992; Tolk
15 et al., 2006), and therefore does not appear to be significant.

16 The overarching aim of this study is to develop an approach that would help in the upscaling
17 of ET_i (retrieved at satellite overpass time) to ET_d . Additional value of this study also consists
18 of exploiting R_{Si} information at satellite local crossing time to predict R_{Sd} which is not directly
19 retrievable from any polar orbiting satellites, so that the ratio of R_{Sd}/R_{Si} can be further used to
20 upscale ET_i to obtain ET_d estimates. Currently we are limited to demonstrating with MODIS
21 satellite overpass times (Terra and Aqua), however for the future missions with different local
22 overpass time, the method would still be applicable.

23 In any natural ecosystem, R_S on a particular day is primarily influenced by the cloud
24 (especially cloud cover fraction and optical thickness) (Mallick et al., 2015; Hildebrandt et al.,
25 2007), latitude, season, and time-of-day. Therefore, R_{Sd} on any specific day is expected to be a
26 function of R_{Si} (as a representative of R_S and cloudiness factors), solar zenith angle
27 (representing latitude, season, time-of-day), day length (representing latitude and season), and
28 $R_{S}TOA$ (representing latitude, season, time-of-day). Besides, atmospheric aerosols also
29 interact with R_S and absorb some of the radiation particularly in the urban areas. Considering
30 the applications of ET_i to ET_d modeling in the natural ecosystems, we include R_{Si} , $R_{Si}TOA$,
31 $R_{Sd}TOA$, solar zenith angle and day length for R_{Sd} (and subsequently ET_d) prediction.

1 2.2 Development of Artificial Neural Network (ANN)

2 ANN is a non-linear model which works by initially understanding the behaviour of a system
3 based on a combination of a given number of inputs and subsequently is able to simulate the
4 system when fed with independent set of inputs of the same system. ANN approach has been
5 successfully used in estimating global solar radiation in many sectors and more so in the field
6 of renewable energy (Ahmad et al., 2015; Hasni et al., 2012; Lazzús et al., 2011). Multi-layer
7 perceptron (MLP) is one of the ANN architectures commonly used as opposed to other
8 statistical methods, makes no prior assumptions concerning the data distribution, has ability to
9 reasonably handle non-linear functions and reliably generalise independent data when
10 presented (Gardner & Dorling, 1998; Khatib, Mohamed, & Sopian, 2012; Wang, 2003). In the
11 present study, MLP was chosen as it has been widely used in many similar studies and cited
12 to be a better alternative as compared to the conventional statistical methods (Ahmad et al.,
13 2015; Chen et al., 2013; Dahmani et al., 2016; Mubiru & Banda, 2008). The MLP is
14 composed of 5 neurons in the input layer, 1 output layer and 10 hidden layers (Fig. 2). The
15 input layer neurons are made up of instantaneous incoming short wave radiation (R_{Si}),
16 instantaneous exo-atmospheric shortwave radiation (R_{SiTOA}), daily exo-atmospheric
17 shortwave radiation (R_{SdTOA}), solar zenith angle (θ_z), and day length (L_D) as the predictor
18 variables whose values are initially standardized to range between -1 to 1. The choice of the
19 inputs is intentionally limited to the variables that cannot only be acquired by measurements
20 from meteorological stations but also derived from simple astronomical computations (Ryu et
21 al., 2012) mainly to help minimize on the spatial distribution problem (as described earlier in
22 the introduction) that is often linked to ground weather stations. In the MLP processing, the
23 input layer directs the values of each input neuron x_i ($i = 1, 2, 3 \dots n$) into each neuron (j) of
24 the hidden layers. In the hidden layer, x_i is multiplied by a weight (w_{ij}) followed by a bias (b_j)
25 assigned for each hidden layer also is applied. The weighted sum (eq. (2)) is fed into a
26 transfer function. In this work a tangent sigmoid (TANSIG) function is used (eq. (3)) in the
27 hidden layer while in the output layer a PURELIN function is applied (eq. (4)) to give a single
28 output value which is the predicted daily shortwave radiation (R_{Sd_pred}). PURELIN is a linear
29 neural transfer function used in backpropagation network. It calculates a layer's output from
30 its net input. The function generates outputs between zero and 1 as the neuron's net input goes
31 from negative to positive infinity. The training of the ANN is completed by a regression

1 analysis being performed internally by the algorithm between the target variable i.e. the
 2 observed and predicted daily shortwave radiation (R_{Sd_obs} and R_{Sd_pred}).

$$x_j = \int \left(\sum_{i=1}^n w_{ij} y_i b_j \right) \quad (2)$$

$$y_j = \frac{2}{(1 + \exp(-2X_i) - 1)} \quad (3)$$

$$y_j = X_i(PURELIN) \quad (4)$$

3 Bayesian regularization algorithm was chosen for the optimization process because it is able
 4 to handle noisy datasets by continuously applying adaptive weight minimization and can
 5 reduce or eliminate the need for lengthy cross-validation that often leads to overtraining and
 6 overfitting of models (Burden and Winkler, 2009).

7 **2.3 Datasets**

8 Daily and half-hourly data on R_s ($W m^{-2}$), R_{STOA} , net radiation (R_n , $W m^{-2}$), latent heat flux
 9 (λE , $W m^{-2}$), sensible heat flux (H , $W m^{-2}$) and ground heat flux (G , $W m^{-2}$) measured by the
 10 FLUXNET (Baldocchi et al., 2001) eddy covariance network were used. A total of 126 sites
 11 from the years 1999 to 2006 distributed between latitude 0-90 degrees north and south of the
 12 equator were used for the present analysis. The data sites covered a broad spectrum of
 13 vegetation functional types and climatic conditions and a list of the sites are given in Table S1
 14 in the supplementary section.

15 Among 126 sites, 85 sites were used for training and remaining 41 sites were used for
 16 validation. Partition of the data into training and validation was randomly selected regardless
 17 of the year. These translated into 194 and 86 yearly data for the respective sample. A global
 18 distribution of the data sites is shown in Fig. 3. From the training dataset, three samples were
 19 internally generated by the algorithm i.e., training datasets, validation datasets, and a testing
 20 dataset in a percentage ratio of 80:15:5 respectively. The ANN algorithm is designed to
 21 validate its performance for any given training which in most cases should be sufficient for
 22 validating the network. However to ensure the network is robust, we further test the generated
 23 network with independent dataset. Considering the equatorial crossing time of different polar

1 orbiting sensors like LANDSAT, ASTER, and MODIS Terra-Aqua, unique networks were
 2 generated for different time of day from morning to afternoon, and thus we had a total of 8
 3 networks to represent potential satellite overpass times between 1030 to 1400 hours using 30
 4 minutes interval as the closest reference time for each hour. The generated networks were
 5 then applied to an independent validation data set.

6 **2.4 Intercomparison of ET_i upscaling methods**

7 An intercomparison of three different ET_i upscaling methods is performed with the
 8 homogeneous datasets to assess their relative performance across a range of temporal scales
 9 and variable sky conditions. These are: (a) R_S -based upscaling method, where ANN predicted
 10 R_{Sd} is used in conjunction with observed R_{Si} to predict ET_d using eq. (1).

11 (b) The exo-atmospheric irradiance method (Ryu et al., 2012) where the reference variable is
 12 $R_S TOA$.

$$R_{Sd} TOA = S_{sc} \left[1 + 0.033 \cos \left(\frac{2\pi t_d}{365} \right) \right] \cos \theta_Z \quad (5)$$

$$SF_{RTOA} = \frac{R_{Sd} TOA}{R_{Si} TOA} \quad (6)$$

$$ET_d = ET_i SF_{RTOA} \quad (7)$$

13 Where S_{sc} is the solar constant (1360 W m^{-2}), t_d is the day of year (DoY), and θ_Z is the solar
 14 zenith angle.

15 (c) EF -based method (Cammalleri et al., 2014), where reference variable is the net available
 16 energy (ϕ) (i.e., $R_n - G$).

$$SF_{EF} = \frac{ET_i}{(R_n - G)_i} \quad (8)$$

$$ET_d = 1.1(R_n - G)_d SF_{EF} \quad (9)$$

17 Where SF_{EF} is the EF -based scaling factor, $(R_n - G)_i$ and $(R_n - G)_d$ are the instantaneous and
 18 daily net available energy, respectively.

1 We tested the performance of the three upscaling algorithms for all possible sky conditions
 2 assumed to be represented by daily atmospheric transmissivity (τ_d) (eq. 10) namely (i)
 3 $0.25 \geq \tau \geq 0$ (τ_1 , hereafter), (ii) $0.5 \geq \tau \geq 0.25$ (τ_2 , hereafter) (iii) $0.75 \geq \tau \geq 0.5$ (τ_3 , hereafter), and (iv)
 4 $1 \geq \tau \geq 0.75$ (τ_4 , hereafter), respectively. We use daily τ because it indicates the overall sky
 5 condition throughout a day.

$$\tau_d = \frac{R_{Sd}}{R_{Sd}TOA} \quad (10)$$

6 R_{Sd} and $R_{Sd}TOA$ are daily shortwave radiation and the exo-atmospheric shortwave radiation in
 7 $\text{MJ m}^{-2} \text{d}^{-1}$ (converted from W m^{-2}).

8 **2.5 Statistical error analysis**

9 The relative performance of the ANN and three upscaling methods is evaluated using
 10 statistical indices generated namely: coefficient of determination (R^2), root mean square error
 11 (RMSE), mean absolute percentage error (MAPE), index of agreement (IA), and bias. ET_d
 12 estimates using the respective upscaling coefficients were compared with measured ET_d .

$$13 \quad R^2 = 1 - \frac{\sum_{i=1}^n (p_i - o_i)^2}{\sum_{i=1}^n (o_i)^2} \quad (11)$$

$$14 \quad RMSE = \sqrt{\frac{\sum_{i=1}^n (o_i - p_i)^2}{n}} \quad (12)$$

$$15 \quad MAPE = \frac{1}{n} \sum_{i=1}^n \frac{|o_i - p_i|}{n} * 100 \quad (13)$$

$$16 \quad IA = \frac{\sum_i (p_i - o_i)^2}{\sum_{i=1}^n (|p_i - o_i| + |o_i - p_i|)^2} \quad (14)$$

$$17 \quad Bias = \frac{\sum_{i=1}^n (p_i - o_i)}{n} \quad (15)$$

1 Where, n is the number of data points; o_i and p_i are daily observed and estimated R_{Sd} or ET_d ,
2 respectively. \bar{O} was the mean value of observed R_{Sd} or ET_d .

3 **2.6 Sensitivity of ANN training and validation**

4 Given the majority of the FLUXNET sites represent forest biomes and the distribution of EC
5 sites over non-forest biomes are proportionately lower as compared to the forests, we
6 performed a sensitivity analysis of the ANN-based approach by assessing the error statistics
7 (R^2 and RMSE) of predicted ET_d for different scenarios of ANN training. Three case studies
8 were generated: (a) Case1, where ANN was trained by including data randomly from the
9 forests and ET_d validation was done in non-forest biomes (i.e., grassland, crops and
10 shrublands); (b) Case2, where ANN was trained by including data randomly from the non-
11 forest biomes and predicted ET_d was evaluated in forest biome; (c) ANN was trained by using
12 data randomly from equal proportions of forest and non-forest biomes, and ET_d validation was
13 also done in forest and non-forest biomes. Each individual case was replicated 10 times and
14 an ensemble mean statistics of predicted ET_d is reported in section 3.5.

15 **3 Results and discussion**

16 **3.1 Testing the performance of predicted R_{Sd}**

17 Given that the performance of ET_d upscaling depends on the soundness of R_{Sd} estimation, we
18 first evaluate the efficacy of the ANN method for predicting R_{Sd} . Figure 4 summarises the
19 statistical results of predicted R_{Sd} (R_{Sd_pred} , hereafter) including all the site-year average R^2 ,
20 RMSE, IA, and MAPE values for eight different time-of-day upscaling time slots. The RMSE
21 of R_{Sd_pred} from forenoon upscaling varied between 1.81-1.85 MJ m⁻² d⁻¹, with MAPE, R^2 , IA
22 varying between 20–21%, 0.76–0.77, and 0.79 and 0.80, respectively (Fig. 4). For the
23 afternoon, these statistics were almost similar and varied between 1.83–1.96 MJ m⁻² d⁻¹, 19-
24 20%, 0.75–0.77, and 0.80–0.81 (Fig. 4). Given the minimal discrepancy in error statistics
25 from both forenoon and afternoon integration and considering the MODIS Terra-Aqua
26 average overpass time we have considered 1100 and 1330 hours of daytime for the detailed
27 follow up analysis.

28 Figure 5 (a, b) evaluates R_{Sd_pred} statistics under different level of atmospheric transmissivity
29 (τ) ($0.25 \geq \tau \geq 0$, $0.5 \geq \tau \geq 0.25$, $0.75 \geq \tau \geq 0.5$, and $1 \geq \tau \geq 0.75$) with an overall RMSE of 1.81 and

1 1.83 MJ m⁻² d⁻¹ for the forenoon and afternoon upscaling respectively. Table 1 and Fig. 5
2 clearly show an overestimation tendency of the current method under persistent cloudy sky
3 conditions (τ_1), whereas the predictive capacity of the ANN model is reasonably strong with
4 increasing atmospheric clearness. The RMSE of R_{Sd_pred} for different τ class from forenoon
5 upscaling varied between 0.62 to 2.45 MJ m⁻² d⁻¹, with MAPE, R² and IA of 9.2 to 53%, 0.67
6 to 0.98, and 0.67 to 0.95, respectively (Table 1). For the afternoon upscaling these statistics
7 were 0.89 to 2.4 MJ m⁻² d⁻¹ (RMSE), 2.4 to 52% (MAPE), 0.65 to 0.98 (R²), and 0.67 to 0.95
8 (IA) (Table 1).

9 The overestimation of R_{Sd_pred} at low values of τ is presumably associated with varying levels
10 of cloudiness during the daytime. Since R_{Sd_pred} depends on the magnitude of R_{Si} , L_D , θ_Z ,
11 R_{SiTOA} , and R_{SdTOA} , there will be a tendency of overestimating R_{Sd_pred} on partly cloudy days if
12 R_{Si} at a specific time-of-day is not affected by the clouds (L_D , θ_Z , R_{SiTOA} , and R_{SdTOA} are not
13 influenced by the clouds).

14 **3.2 Evaluation of predicted ET_d based on R_{Sd_pred}**

15 Figure 6 summarises the statistical results of predicted ET_d (ET_{d_pred} , hereafter) for eight
16 different time-of-day slots. Upon statistical evaluation, all the cases showed significantly
17 linear relationship between ET_{d_pred} and observed ET_d (ET_{d_obs} , hereafter). The RMSE of
18 ET_{d_pred} from forenoon upscaling varied from 1.67–1.84 MJ m⁻² d⁻¹, with MAPE, R², IA
19 varying between 30%–34%, 0.62–0.68, and 0.77–0.80, respectively (Fig. 6). For the afternoon
20 upscaling, these statistics varied between 1.5–1.6 MJ m⁻² d⁻¹, 29%–30%, 0.67–0.71, and 0.80
21 (Fig. 6). These results also indicate that the error statistics were nearly uniform and the
22 accuracy of ET_{d_pred} varied only slightly when integration was done from different time-of-
23 day hours between 1030 to 1400 h. These typical error characteristics can greatly benefit the
24 ET_d modelling using polar orbiting data with varying overpass times between 1030 to 1400
25 hours. This also opens up the possibility to use either forenoon satellite (e.g., MODIS Terra,
26 LANDSAT, ASTER etc.) or afternoon satellite (i.e., MODIS Aqua) to upscale ET_i to ET_d .
27 Following R_{Sd} , here also we restricted our analysis to the two different time-of-day (1100h
28 and 1330h) representing Terra and Aqua overpass times.

1 Figure 7 (a and b) compares ET_{d_pred} against ET_{d_obs} for different level of daily τ . The overall
2 RMSE, MAPE, and R^2 were 1.86 and 1.55 $\text{MJ m}^{-2} \text{d}^{-1}$, 31% and 36%, 0.65 and 0.69 for the
3 forenoon and afternoon upscaling, respectively. As seen in Fig. 7, there is a systematic
4 overestimation of ET_{d_pred} relative to the tower observed values for low range of τ (i.e., cloudy
5 sky). It is important to realise that, unlike ET_{d_obs} , ET_{d_pred} might be an outcome of ET_i
6 instances when the sky was not overcast, i.e., the sky conditions might be clear at specific
7 time-of-day but can be substantially overcast for the remainder of the daytime. As a result,
8 any bias in the daily shortwave radiation prediction (R_{Sd_pred}) will result in biased ET_{d_pred}
9 according to eq. 1, and the omission of non-clear sky conditions at any particular time of
10 daytime would tend to lead to $ET_{d_pred} > ET_{d_obs}$ for generally overcast days. However, there
11 could be another opposite case that sky is cloudy at e.g., 1100 hr but clear at other times. This
12 will probably lead to an underestimation of R_{Sd_pred} , and consequently underestimation of
13 ET_{d_pred} . Such cases were also found in τ_3 categories in Fig. 7 where clouds of data points
14 clearly falling significantly below the 1:1 line, thus showing substantial underestimation of
15 ET_{d_pred} . Since ET_{d_obs} are the integrations of multiple ET_i measurements, such conditions
16 could be conveniently captured in the observations which were not possible in the current
17 framework of ET_{d_pred} . Therefore, when upscaling was done under clear skies at nominal
18 acquisition time for generally overcast days, higher errors in ET_{d_pred} can be expected
19 (Cammalleri et al., 2014) and vice-versa. We examined this cloudy sky overestimation pattern
20 in greater detail by evaluating the error statistics in ET_{d_pred} for four different levels of daily τ
21 categories (Fig. 8).

22 Statistical evaluation of ET_{d_pred} for different classes of daily τ (estimated as the ratio between
23 daily observed R_{Sd} and R_{SdTOA}) indicates the tendency of higher RMSE and low R^2 in
24 ET_{d_pred} under the persistent cloudy-sky conditions (τ_1), while the performance of ET_{d_pred} is
25 reasonably good with increasing atmospheric clearness (τ_2 , τ_3 , and τ_4) (Fig. 8). The RMSE of
26 ET_{d_pred} for different τ class from forenoon upscaling varied between 1.09 to 2.96 $\text{MJ m}^{-2} \text{d}^{-1}$,
27 with MAPE, R^2 and IA of 25 to 75%, 0.38 to 0.79, and 0.71 to 0.82, respectively. For the
28 afternoon upscaling, these statistics were 0.98 to 2.02 $\text{MJ m}^{-2} \text{d}^{-1}$ (RMSE), 24 to 87%
29 (MAPE), 0.40 to 0.68 (R^2), and 0.71 to 0.77 (IA).

1 To probe into detail of the high errors under persistent cloudiness conditions, a new ANN was
2 trained by introducing daily precipitation (P) and soil moisture (SM) information (along with
3 R_S , $R_{S\text{TOA}}$, θ_z , and L_D) assuming that the inclusion of these two variables might improve the
4 predictive power of R_S -based ANN. In the new ANN, we used data from the sites where
5 coincident measurements of P and S_M were available along with R_S and ET , and validated ET_d
6 predictions of the new ANN on independent sites. The analysis revealed 34% reduction in
7 RMSE (from 3.28 to 2.88 MJ m⁻² d⁻¹), 16% reduction in MAPE (from 90 to 76%), and 49%
8 reduction in mean bias (0.76 to 0.39 MJ m⁻² d⁻¹) for persistent cloudy-sky cases (i.e., τ_1
9 scenarios) from 1100 hr upscaling. However, no significant improvements in ET_{d_pred} were
10 evident for τ_2 , τ_3 , and τ_4 and also for any of the τ classes from the afternoon (1330 hr)
11 upscaling (Fig. 9). ET_d is generally controlled by radiation and soil moisture availability.
12 Under the radiation controlled conditions, ET_d is generally not limited due to soil moisture
13 and 70 – 75% of the net radiation is contributed to ET_d . Therefore, R_S -based method of ET_i
14 upscaling is expected to perform reasonably well unless the upscaling is performed from a
15 clear sky instance for a predominantly overcast or rainy day. However, from Fig. 9 is it
16 apparent that the inclusion of cloud information (cloud fraction, cloud optical thickness) in
17 R_S -based ANN would substantially reduce ET_{d_pred} errors when upscaling is performed from a
18 clear sky instance for a predominantly overcast day and vice-versa. Improvements of ET_{d_pred}
19 error statistics by including daily P and SM (as an indicator of cloudiness) is also suggestive
20 to the relevance of such approach as a future improvement of the current framework, which is
21 expected to reduce the systematic error under overcast conditions. However, the cloud
22 information available from alternative sources e.g., from the Clouds and Earth's Radiant
23 Energy System (CERES), the International Satellite Cloud Climatology Project–Flux Data
24 (ISCCP-FD), and Global Energy and Water cycle Experiment Surface Radiation Budget
25 (GEWEX-SRB) are available at coarse spatial resolution (100 km²) and combining these
26 information with EC tower measurements to train ANN could also introduce additional errors
27 due to the spatial scale mismatch, is therefore out of scope of the present study.

28 Figure 10 shows the time series comparisons between observed ET_d and ET_{d_pred} for four
29 different stations representing different latitude bands of both the Northern (Sweden) and
30 Southern (Brazil, Australia, and South Africa) hemispheres. These reveal that the temporal
31 dynamics of ET_d is in general consistently captured by the proposed method throughout year.

1 In Br_SP1, relatively less seasonality was found in both observed and predicted ET_d . This is
2 because SP1 is a tropical site having an annual rainfall of 850–1100 mm most of which is
3 evenly distributed between March to end of September. The peaks in ET_d values during the
4 beginning of year and October onwards coincided with the periods of increased R_S , and
5 ET_{d_pred} could reasonably capture the observed trends during both rainy and non-rainy
6 periods. Similarly the low ET_d pattern (0.1 to 2 MJ m⁻² d⁻¹) in the hot arid climate of South
7 Africa (Za-Kru) could also be reasonably captured in ET_{d_pred} (Fig. 10). ET_{d_pred} in the other
8 Southern hemisphere (AU-Tum) and Northern hemisphere (SE-Fla) sites have shown distinct
9 seasonality (high summer and low winter ET_d) coinciding with the observed ET_d patterns.

10 **3.3 Comparison with existing ET upscaling methods**

11 ET_{d_pred} from R_S -based method was intercompared with two other upscaling schemes ($R_S TOA$
12 and EF) over 41 FLUXNET validation sites for two different time-of-day, 1100h and 1330h,
13 the statistics of which are given in Table 2. This comparison was also carried out according to
14 different τ classes as defined in section 2.2.3.

15 From Table 2 it is apparent that the R_S -based method has generally produced relatively low
16 RMSE (1.21 to 1.99 MJ m⁻² d⁻¹) and MAPE (23 to 50%) as well as relatively high IA (0.72 to
17 0.84) as compared to $R_S TOA$ and EF -based upscaling methods. The EF -based upscaling
18 method appears to systematically underestimate ET_d for both forenoon and afternoon as
19 evident from high negative bias compared to the other two methods (Table 2). On comparing
20 R_S and $R_S TOA$ methods, R_S -based method performed relatively better than the $R_S TOA$ scheme
21 for low magnitude of τ (i.e., under predominantly cloudy-sky). However, the results suggest
22 comparable performance of $R_S TOA$ -based approach under clear sky conditions which are
23 reflected in lowest RMSE (1.09 and 1.13 MJ m⁻² d⁻¹) in ET_{d_pred} as compared to the other τ
24 classes. In general, all the schemes performed relatively better from the afternoon upscaling as
25 compared to the morning upscaling (as evidenced in higher R^2 and lower bias) (Table 2)
26 which is in agreement with the findings from Ryu et al. (2012). Due to their comparable error
27 statistics, an intercomparison of R_S and $R_S TOA$ -based methods of ET_i upscaling was also
28 carried out across different biomes.

29 Biome specific evaluation of R_S -based ET_{d_pred} (Fig. 11) revealed lowest RMSE and highest
30 R^2 both in the grassland (GRA) (0.68 to 1.14 MJ m⁻² d⁻¹; 0.53 to 0.79) and shrubland (SH)

1 (0.66 to 1.76 MJ m⁻² d⁻¹; 0.60 to 0.82) whereas the RMSE was comparatively high over the
2 tropical evergreen broadleaf forests (EBF) (1.41 to 2.02 MJ m⁻² d⁻¹) and deciduous broadleaf
3 forests (DBF) (1.94 to 2.55 MJ m⁻² d⁻¹). Similar evaluation with *R_sTOA*-based method
4 revealed the lowest RMSE and highest R² in the grassland (0.64 to 1.14 MJ m⁻² d⁻¹; 0.61 to
5 0.84), and highest RMSE in EBF, DBF, and evergreen needleleaf forests (ENF) (1.57 to 2.05
6 MJ m⁻² d⁻¹, 1.2 to 2.25 MJ m⁻² d⁻¹ and 0.93 to 4.02 MJ m⁻² d⁻¹) (Fig. 11c and 11d). Higher
7 *ET_{d,pred}* errors in forests are related to the predominant cloudy-sky issue as described earlier.
8 Tropical evergreen broadleaf forests (and forests in general) have high *ET*, water tends to re-
9 cycle locally and generate rainfall. Therefore, cloudy sky conditions are more frequent at
10 tropical evergreen broadleaf forest and other forests types than at grassland and shrublands. In
11 the biome specific *ET_{d,pred}* error statistics (Fig. 11), relatively large bias in crop *ET_{d,pred}* is
12 introduced due to the inclusion of irrigated agroecosystems in the validation. In irrigated
13 agroecosystems, day-to-day variation in soil moisture is not substantial and *ET_d* is
14 predominantly controlled by the net radiation. Therefore, the inclusion of soil moisture in the
15 current ANN framework is unlikely to improve *ET_{d,pred}* statistics in the irrigated
16 agroecosystems. Further having many explanatory variables (e.g., land management,
17 irrigation statistics, anthropogenic factors) to train the ANN, we risk overfitting the model and
18 hence introducing bias. It is also evident that both *R_s* and *R_sTOA*-based method of *ET_d*
19 estimation would be better suited for natural ecosystem e.g., in the Amazon basin or in the
20 forest ecosystems where significant hydrological and climatological projections are
21 emphasizing the role of *ET_d* to understand the resilience of natural ecosystems in the spectre
22 of hydro-climatological extremes (Harper et al., 2014; Kim et al., 2012). The performance of
23 the method in the semi-arid shrublands appear to be promising (Fig. 11) and therefore the
24 method seems to be credible under water-stressed environment also.

25 Given this analysis was based on FLUXNET sites distributed across 0-90 degrees latitude
26 north and south, the training datasets covers substantial climatic and vegetation variability.
27 The percentage distribution of the training data according to vegetation type was; 23% crops,
28 31% deciduous broadleaf forest, 10% evergreen broadleaf forest, 20% evergreen need leaf
29 forest, 8% grassland, 7% shrubs and 1% aquatic as indicated in table S1. The number of
30 grassland and shrubs as indicated were relatively less as compared to the crops and forests
31 sites. However, biome specific error statistics (Fig. 11) indicted the absence of any systematic

1 errors due to vegetation sampling with the exception of EBF. Availability of more EBF sites
2 in the training datasets is expected to reduce the cloudy-sky errors substantially, due to the
3 assimilation of more cloud information into the R_S -based ANN training.

4 The tendency of positive bias in ET_{d_pred} from both R_S and $R_{S\text{TOA}}$ in clear skies from
5 afternoon upscaling is partly explained by the fact that, during the afternoon the values of
6 both R_S and $R_{S\text{TOA}}$ reached maximum limit and dominates their daily values (Jackson et al.,
7 1983). The post afternoon rate of reduction in ET does not coincide with the shortwave
8 radiation due to stomatal controls on ET , and the total water flux from morning to afternoon
9 (0700h to 1300h) is generally greater than the total water flux from post afternoon (1500h
10 onwards) till sunset. Therefore multiplying 1330h ET_i with high magnitude of R_{Sd}/R_{Si} or
11 $R_{Sd\text{TOA}}/R_{Si\text{TOA}}$ might lead to an overestimation of ET_{d_pred} in the clear sky days.

12 Since extraterrestrial shortwave radiation is not affected by the clouds, ET_{d_pred} from $R_{S\text{TOA}}$
13 performed comparably with the R_S -based ET_{d_pred} with increasing atmospheric clearness (i.e.,
14 for the higher levels of daily τ). However, increased differences in the RMSE of ET_{d_pred}
15 between R_S and $R_{S\text{TOA}}$ upscaling in the predominantly cloudy days indicates that more
16 deviations can be expected in ET_{d_pred} from these two different method of upscaling under
17 principally overcast conditions (Tang et al., 2013). This happens because the ratio of $R_{Sd\text{TOA}}$
18 $/R_{Si\text{TOA}}$ is not impacted by the clouds and the magnitude of this ratio becomes markedly
19 different from R_{Sd}/R_{Si} ratio in the presence of clouds, which leads to the differences in ET_{d_pred}
20 between them. The R_S -based method is relatively efficient to discriminate the impacts on ET
21 by R_{Sd}/R_{Si} due to the clouds. The generally good performance of R_S -based method and
22 comparable error statistics with $R_{S\text{TOA}}$ -based ET_d estimates are consistent with the findings
23 of Cammalleri et al. (2014) and Van Niel et al. (2012). As shown in Table 2, relatively lower
24 RMSE of $R_{S\text{TOA}}$ -based ET_{d_pred} for atmospheric transmissivity class above 0.75 reveals that
25 under pristine clear sky conditions $R_{S\text{TOA}}$ can be successfully used to upscale ET_i . However,
26 one of the main reasons for the differences in RMSE between R_S and $R_{S\text{TOA}}$ method for daily
27 transmissivity above 0.75 could be due to the fact that if ET_i upscaling is performed from a
28 cloudy instance for a predominantly clear sky day, then such RMSE difference between the
29 two different upscaling methods is expected. These results also revealed the probability of a
30 hybrid ET_i upscaling method by combining cloud information or SM and P in R_S -method (for

1 transmissivity between zero to 0.5) and $R_S TOA$ -method (for transmissivity greater than 0.5).
2 However this hypothesis needs to be tested further.

3 The systematic ET_d underestimation by EF -based upscaling method and nearly similar pattern
4 of bias from two different time-of-day upscaling (Table 2) further points to the fact that the
5 concave-up shape of EF during daytime (Hoedjes et al., 2008; Tang et al., 2013) will tend to
6 underestimate ET_d if EF is assumed to be conservative during the daytime. EF remains
7 conservative during the daytime under extremely dry conditions when ET_d is solely driven by
8 deep layer soil moisture. The systematic underestimation of ET_d from EF -based upscaling
9 method corroborates with the results reported by other researchers (Cammalleri et al., 2014;
10 Delogu et al., 2012; Gentine et al., 2007; Hoedjes et al., 2008) which suggests that the self-
11 preservation of EF is not generally achieved, and this systematic underestimation of ET_d can
12 be partially compensated if EF -based ET_i upscaling is done from morning 0900h or afternoon
13 1600h time-of-day.

14 We further resampled ET_d (both predicted and observed) from daily to 8-day, monthly, and
15 annual scale, and statistical metrics from the three different upscaling methods at three
16 different temporal scales are shown in Fig. 12 and Table 3. Averaging ET_d at 8-day, monthly
17 and annual scale substantially reduced the RMSE to the order of 60 to 70% for all the three
18 upscaling methods. The R_S -based upscaled ET_d from morning and afternoon showed reduction
19 in RMSE from 1.79 MJ to 0.57 MJ and 1.74 MJ to 0.51 MJ from daily to annual ET ,
20 respectively. For the other two upscaling method these statistics varied from 1.85 and 1.89 MJ
21 to 0.62 and 0.53 MJ ($R_S TOA$ method), and 2.16 and 1.33 MJ to 2.20 and 1.31 MJ (EF
22 method) (Fig. 12 and Table 3). The impacts of daily cloud variability might have smoothed
23 out in 8-day, monthly and annual scale which led to reduced RMSE and higher correlation
24 between ET_{d_pred} and ET_{d_obs} . Nearly similar error statistics in ET_{d_pred} from both the morning
25 and afternoon upscaling also substantiates the findings of Ryu et al. (2012) and greatly
26 stimulate the use of either morning satellite (i.e., Terra) or after satellite (i.e., Aqua) to upscale
27 ET_i to ET_d or 8-day mean ET_d .

28 The principal limitation of the approach is the dependence of ET_d and R_{Sd} on single snapshot
29 of ET_i and R_{Si} . Although hourly R_S data from geostationary satellite are becoming available;
30 but these are available as sectorial products (i.e. for particular continents) instead of full

1 global coverage. Ongoing efforts to develop geostationary based data by merging multiple
2 geostationary satellites tend to overcome this limitation.

3 **3.4 Impact of energy balance closure on ET_{d_pred}**

4 FLUXNET EC sites have long been identified to be prone to surface energy budget
5 imbalance, which might lead to ($\pm 20\%$) to ($\pm 40\%$) under measurement of latent heat fluxes.
6 In order to assess the impacts of surface energy balance (SEB) closure on current ET_d
7 prediction, we further compared the error statistics of R_S -based ET_{d_pred} (Table 4) for both
8 ‘closed’ and ‘unclosed’ surface energy balance datasets. These are the subsets of the data
9 where all the four SEB components (λE , sensible heat flux, ground heat flux, and net
10 radiation) were available and SEB was closed by the residual SEB closure method (Foken,
11 2006). Table 4 revealed substantially low RMSE (10 to 60%), R^2 (8 to 100%) and MAPE (1
12 to 75%) in ET_{d_pred} when ET_i upscaling is done by ‘unclosed’ SEB. A consistently high
13 positive mean bias (0.63 to 3.83) in ET_{d_pred} with ‘closed’ SEB was also noted (Table 4).
14 Although, various methods exist to close the surface energy balance, but, the impact of
15 various SEB closure methods on ET_{d_pred} statistics is beyond the scope of the current study. It
16 is also important to mention that in the satellite based ET_i retrieval, net available energy is
17 partitioned into ET and sensible heat flux with the implicit assumption of SEB closure.
18 Therefore, application of the current ANN framework is expected not to impact the remote
19 sensing based ET_i to ET_d upscaling. However, for the validation of remote sensing based ET_d
20 retrievals, surface energy balance fluxes from eddy covariance measurements need to be
21 closed.

22 **3.5 Sensitivity of ANN derived ET_{d_pred} to biome selection**

23 A sensitivity analysis of ANN derived R_S -based ET_{d_pred} revealed variable sensitivity of the
24 ANN framework to the biome selection. The coefficient of determination (R^2) varied between
25 0.71 to 0.84 and RMSE between 0.96 to 2.10 MJ m⁻² d⁻¹ across three different scenarios of
26 ANN training and validation (Fig. 13). However, RMSE was found to be relatively high in
27 forests in Case2, where ANN was trained by using the data from crops, grasslands and
28 shrublands only. For the Case1 and Case3, no substantial difference was noted (Fig. 13). This
29 therefore revealed the fact that the inclusion of forests in ANN training leads to lower errors
30 in ET_{d_pred} over non-forest biomes, although the reverse scenario is not likely to be true. Since

1 forests generally have high ET , water recycling tends to be more over the forests which
2 produces substantial rainfall, variable atmospheric water vapor, associated cloudiness, and
3 radiation. Cloudiness is a phenomenon that significantly influences the reliability of a model
4 to predict incoming solar radiation as they are directly related to each other. Therefore, when
5 R_S -based ANN is trained with data from forests, the model assimilates information on a
6 diverse range of radiative forcings which broaden their applicability in other biomes. This
7 also emphasizes the fact that the performance of such ANN-based approach is primarily
8 sensitive to their training over a broad spectrum of atmospheric conditions.

9 **4 Summary and Conclusions**

10 Given the significance of ET_d in remote sensing based water resource management from polar
11 orbiting satellites, this study developed and evaluated a temporal upscaling method for
12 estimating ET_d from different time-of-day instantaneous ET (ET_i) measurements with the
13 assumption that the ratio between daytime to instantaneous shortwave radiation (R_{Sd}/R_{Si}) is the
14 predominant factor governing ET_d/ET_i ratio. However, since R_{Sd} is not directly measurable
15 from the polar orbiting satellites, we trained an ANN with the FLUXNET observations of R_{Si}
16 and R_{Sd} , and validated the model to predict R_{Sd} over independent sites, followed by using
17 R_{Sd}/R_{Si} ratio for converting ET_i to ET_d . The overarching goal of this study is to provide an
18 operational and robust ET_i upscaling protocol for estimating ET_d from any polar orbiting
19 satellite. The datasets used for the ANN model development covers a wide range of biome,
20 climate, and variable sky conditions. Therefore, we assume the R_{Sd} prediction from ANN to
21 capture a broad spectrum of radiative forcing, which is also reflected in the independent
22 validation of R_{Sd} and ET_d (Fig. 5, Fig. 7, Table 2). However, the performance of this model
23 for satellite retrieval of R_{Sd} (from R_{Si}) is dependent on the accuracy of R_{Si} retrieval (Loew et
24 al., 2016). Also, the distribution of sites over the tropics, Africa, and South East Asia are
25 poor, and more sites over these regions are expected to make the ANN model performance
26 more robust.

27 Based on measurements from 126 flux tower sites, we found R_S -based upscaled ET_d to
28 produce a significant linear relation ($R^2 = 0.65$ to 0.69), little bias (-0.31 to -0.56 $\text{MJ m}^{-2} \text{d}^{-1}$)
29 (appx. 4%), and good agreement (RMSE 1.55 to 1.86 $\text{MJ m}^{-2} \text{d}^{-1}$) (appx. 10%) with the
30 observed ET_d . While the exoatmospheric shortwave radiation driven ET_i upscaling method

1 (i.e., $R_S TOA$ -based) appeared to produce slightly lower RMSE (10% lower) under cloud-free
2 conditions (Table 2), global shortwave radiation driven method (i.e., R_S -based method)
3 demonstrates more robust performance and was found to be better under cloudy conditions.
4 Despite R_S -based method yielded relatively better overall accuracy in ET_d prediction (i.e.,
5 ET_{d_pred}) statistics when compared with the $R_S TOA$ and evaporative fraction based (EF -based)
6 method, statistical analysis of ET_{d_pred} accuracy of different temporal upscaling methods (as
7 discussed in section 3.3) suggests that R_S and $R_S TOA$ to produce commensurate results under
8 coarse temporal resolutions (Table 3). Therefore, at the coarse temporal scale (8-day and
9 above), any of these two methods (R_S and $R_S TOA$) can be used for ET_i to ET_d upscaling.

10 The proposed upscaling method is based on the idea that instantaneous ET/R_S approximates
11 daily ET/R_S , although it implicitly includes the stomatal controls on ET observations mediated
12 by the vegetation. The cases where ET_i is low due to water stress induced strong stomatal
13 control; low magnitude of ET will also be reflected in upscaling ET_i to ET_d (according to eq.
14 1). However, to account for any carry over effects of the stomatal control on ET_d , inclusion of
15 longwave radiation would likely to improve the scheme. Stomatal control is significantly
16 dependent on the thermal longwave radiative components, and, therefore, the relative
17 proportion of downwelling and upwelling longwave radiation is expected to be a stomatal
18 constraint. However, the availability of longwave radiation measurement stations in the
19 FLUXNET datasets is limited to formulate ANN and evaluate this hypothesis. In general, the
20 stomatal and biophysical constraints are imposed in state-of-the-art thermal remote sensing
21 based ET_i retrieval schemes, and, therefore the ANN framework can be applied to upscale
22 remote sensing based ET_i to ET_d . Also, relatively good performance of the model in semiarid
23 shrubland also indicated the applicability of the method in water stressed ecosystems where
24 stomatal controls are predominant.

25 Among all the upscaling method tested, R_S -based method carries maximum information on
26 the cloudiness and produced generally lowest RMSE, low bias (Table 3), and, therefore,
27 overall the preferably robust scaling mechanism (at the daily scale) among all the other
28 methods tested. The true added value of the ANN is for an operational ET_d product from polar
29 satellites. Currently, the polar Earth orbiting satellites provide us with ET_i only. However, for
30 most hydrological and ecosystem modeling applications, ET_d is needed. Therefore, for studies
31 that will opt to apply R_S -based method as a scaling algorithm, R_{Sd} will be easily available for

1 any measurement of R_{Si} by the satellite using the ANN. However, upscaling large-area
2 satellite-based ET_i by using retrieved R_{Si} would require accurate R_{Si} retrieval techniques,
3 which are currently commonplace (Ahmad et al., 2015; Boulifa et al., 2015; Dahmani et al.,
4 2016; Hasni et al., 2012; Li, Tang, Wu, & Liu, 2013) to support regional scale hydrological
5 applications. Of the two other upscaling methods, $R_S TOA$ could be easily applied over large
6 areas, had lower errors than EF , had second best RMSE, and overall lowest bias among the
7 two. We conclude that using modelled R_S to upscale ET_i at daily scale appears to be viable for
8 large-area hydrological remote sensing applications from polar orbiting satellites irrespective
9 of any sky conditions.

10 **Acknowledgements**

11 The authors thank HiWET (High resolution modelling and monitoring of water and energy
12 transfers in WETland ecosystems) project funded through the Belgian Science Policy
13 (BELSPO) and FNR under the programme STEREOIII (INTER/STEREOIII/13/03/HiWET)
14 (CONTRACT NR SR/00/301). We thank entire FLUXNET site PIs for sharing the eddy
15 covariance data. This work used eddy covariance data acquired by the FLUXNET community
16 and in particular by the following networks: AmeriFlux (U.S. Department of Energy,
17 Biological and Environmental Research, Terrestrial Carbon Program (DE-FG02-04ER63917
18 and DE-FG02-04ER63911)), AfriFlux, AsiaFlux, CarboAfrica, CarboEuropeIP, CarboItaly,
19 CarboMont, ChinaFlux, Fluxnet-Canada (supported by CFCAS, NSERC, BIOCAP,
20 Environment Canada, and NRCan), GreenGrass, KoFlux, LBA, NECC, OzFlux, TCOS-
21 Siberia, USCCC. We acknowledge the financial support to the eddy covariance data
22 harmonization provided by CarboEuropeIP, FAO-GTOS-TCO, iLEAPS, Max Planck Institute
23 for Biogeochemistry, National Science Foundation, University of Tuscia, Université Laval,
24 Environment Canada and US Department of Energy and the database development and
25 technical support from Berkeley Water Center, Lawrence Berkeley National Laboratory,
26 Microsoft Research eScience, Oak Ridge National Laboratory, University of California–
27 Berkeley and the University of Virginia. LW acknowledges the PhD supervision from Dr.
28 Wout Verhoef and Dr. Christian van der Tol from University of Twente, The Netherlands.

1 KM designed the analysis, LW performed the research, KM and LW developed the
2 manuscript, and all the coauthors jointly contributed in editing the manuscript. The authors
3 declare no conflict of interest.

4

1 **References**

- 2 Ahmad, A., Anderson, T. N., and Lie, T. T.: Hourly global solar irradiation forecasting for
3 New Zealand, *Sol. Ener.*, 122, 1398–1408, doi:10.1016/j.solener.2015.10.055, 2015.
- 4 Allen, R. G., Pereira, L. S., Raes, D., and Smith, M.: Crop evapotranspiration, Guidelines for
5 computing crop water requirements, FAO Irrigation and drainage paper n. 56. 326 pp.,
6 Rome, Italy, 1998.
- 7 Anderson, R. G., Lo, M.-H., Swenson, S., Famiglietti, J. S., Tang, Q., Skaggs, T. H., Lin, Y.-
8 H., and Wu, R.-J.: Using satellite-based estimates of evapotranspiration and groundwater
9 changes to determine anthropogenic water fluxes in land surface models, *Geosci. Model*
10 *Dev.*, 8, 3021-3031, doi:10.5194/gmd-8-3021-2015, 2015.
- 11 Baigorria, G. A., Villegas, E. B., Trebejo, I., Carlos, J. F., and Quiroz, R.: Atmospheric
12 transmissivity: distribution and empirical estimation around the central Andes, *Int. J.*
13 *Climatol.*, 24 (9), 1121–1136, doi:10.1002/joc.1060, 2004.
- 14 Baldocchi, D.D., Falge, E., Gu, L., Olson, R., Hollinger, D., Running, S., et al.: Fluxnet: a
15 new tool to study the temporal and spatial variability of ecosystem-scale carbon dioxide,
16 water vapor, and energy flux densities, *Bull. American Met. Soc.*, 82 (11), 2415–3434,
17 doi:10.1175/1520-0477(2001)082<2415:FANTTS>2.3.CO;2, 2001.
- 18 Bisht, G., Venturini, V., Islam, S., and Jiang, L.: Estimation of the net radiation using MODIS
19 (Moderate Resolution Imaging Spectroradiometer) data for clear sky days, *Remote Sens.*
20 *Environ.*, 97 (1), 52–67, doi:10.1016/j.rse.2005.03.014, 2005.
- 21 Boulifa, M., Adane, A., Rezagui, A., and Ameer, et. Z.: Estimate of the Global Solar
22 Radiation by Cloudy Sky Using HRV Images, *Ener. Proc.*, 74, 1079–1089,
23 doi:10.1016/j.egypro.2015.07.747, 2015.
- 24 Brutsaert, W., and Sugita, M.: Application of self-preservation in the diurnal evolution of the
25 surface energy budget to determine daily evaporation, *J. Geophys. Res. Atmos.*, 97
26 (D17), 18377–18382, doi: 10.1029/92JD00255, 1992.
- 27 Burden, F., and Winkler, D.: Bayesian Regularization of Neural Networks. In D. Livingstone
28 (Ed.), *Artificial Neural Networks SE - 3*, 458, 23–42, Humana Press, doi:10.1007/978-1-
29 60327-101-1_3, 2009.
- 30 Cammalleri, C., Anderson, M. C., and Kustas, W. P.: Upscaling of evapotranspiration fluxes
31 from instantaneous to daytime scales for thermal remote sensing applications, *Hydrol.*
32 *Earth Sys. Sci.*, 18 (5), 1885–1894, doi:10.5194/hess-18-1885-2014, 2014.
- 33 Chávez, J. L., Neale, C. M. U., Prueger, J. H., and Kustas, W. P.: Daily evapotranspiration
34 estimates from extrapolating instantaneous airborne remote sensing ET values, *Irrig.*
35 *Sci.*, 27 (1), 67–81, doi:10.1007/s00271-008-0122-3, 2008.
- 36 Chen, Z., Shi, R., and Zhang, S.: An artificial neural network approach to estimate

- 1 evapotranspiration from remote sensing and AmeriFlux data, *Front. Earth Sci.*, 7 (1),
2 103–111, doi:10.1007/s11707-012-0346-7, 2013.
- 3 Colaizzi, P. D., Evett, S. R., Howell, T. A., and Tolck, J. A.: Comparison of five models to
4 scale daily evapotranspiration from one-time-of-day measurements, *Trans. ASAE*, 49,
5 1409–1417, doi: 10.13031/2013.22056, 2006.
- 6 Crago, R. D.: Conservation and variability of the evaporative fraction during the daytime, *J.*
7 *Hydrol.*, 180 (1–4), 173–194, doi:10.1016/0022-1694(95)02903-6, 1996.
- 8 Dahmani, K., Notton, G., Voyant, C., Dizene, R., Nivet, M. L., Paoli, C., and Tamas, W.:
9 Multilayer Perceptron approach for estimating 5-min and hourly horizontal global
10 irradiation from exogenous meteorological data in locations without solar measurements,
11 *Ren. Ener.*, 90, 267–282. doi:10.1016/j.renene.2016.01.013, 2016.
- 12 Delogu, E., Boulet, G., Oliosio, A., Coudert, B., et al.: Reconstruction of temporal variations
13 of evapotranspiration using instantaneous estimates at the time of satellite overpass,
14 *Hydrol. Earth Syst. Sci.*, 16 (8), 2995–3010, doi:10.5194/hess-16-2995-2012, 2012.
- 15 Foken, T., Wimmer, F., Mauder, M., Thomas, C., and Liebethal, C.: Some aspects of the
16 energy balance closure problem, *Atm. Chem. Phys.*, 6 (12), 4395–4402,
17 doi:10.5194/acp-6-4395-2006, 2006.
- 18 Franssen, H. J. H., Stöckli, R., Lehner, I., Rotenberg, E., and Seneviratne, S. I.: Energy
19 balance closure of eddy-covariance data: A multisite analysis for European FLUXNET
20 stations, *Agric. For. Meteorol.*, 150 (12), 1553–1567,
21 doi:10.1016/j.agrformet.2010.08.005, 2010.
- 22 Gardner, M. W., and Dorling, S. R.: Artificial neural networks (the multilayer perceptron)—a
23 review of applications in the atmospheric sciences, *Atmos. Environ.*, 32 (14–15), 2627–
24 2636, doi:10.1016/S1352-2310(97)00447-0, 1998.
- 25 Gentine, P., Entekhabi, D., Chehbouni, A., Boulet, G., and Duchemin, B.: Analysis of
26 evaporative fraction diurnal behaviour, *Agric. For. Meteorol.*, 143 (1–2), 13–29,
27 doi:10.1016/j.agrformet.2006.11.002, 2007.
- 28 Harper, A., Baker, I. T., Denning, A. S., Randall, D. A., Dazlich, D., and Branson, M.: Impact
29 of Evapotranspiration on Dry Season Climate in the Amazon Forest, *J. Clim.*, 27 (2),
30 574–591, doi: 10.1175/JCLI-D-13-00074.1, 2014.
- 31 Hasni, A., Sehli, A., Draoui, B., Bassou, A., and Amieur, B.: Estimating Global Solar
32 Radiation Using Artificial Neural Network and Climate Data in the South-western
33 Region of Algeria, *Energy Proc.*, 18, 531–537, doi:10.1016/j.egypro.2012.05.064, 2012.
- 34 Hildebrandt, A., Aufi, M. A., Amerjeed, M., Shammass, M., and Eltahir, E. A. B.:
35 Ecohydrology of a seasonal cloud forest in Dhofar: 1. Field experiment, *Water Resour.*
36 *Res.*, 43, W10411, doi:10.1029/2006WR005261, 2007.
- 37 Hoedjes, J. C. B., Chehbouni, A., Jacob, F., Ezzahar, J., and Boulet, G.: Deriving daily

- 1 evapotranspiration from remotely sensed instantaneous evaporative fraction over olive
2 orchard in semi-arid Morocco, *J. Hydrol.*, 354 (1–4), 53–64,
3 doi:10.1016/j.jhydrol.2008.02.016, 2008.
- 4 Huang, G., Liu, S., and Liang, S.: Estimation of net surface shortwave radiation from MODIS
5 data, *Int. J. Remote Sens.*, 33 (3), 804–825, doi:10.1080/01431161.2011.577834, 2012.
- 6 Jackson, R. D., Hatfield, J. L., Reginato, R. J., Idso, S. B., and Pinter, P. J. Jr.: Estimation of
7 daily evapotranspiration from one time-of-day measurements, *Agric. Wat. Man.*, 7 (1–3),
8 351–362, doi:10.1016/0378-3774(83)90095-1, 1983.
- 9 Khatib, T., Mohamed, A., and Sopian, K.: A review of solar energy modeling techniques,
10 *Ren. Sust. Energy Rev.*, 16 (5), 2864–2869, doi: 10.1016/j.rser.2012.01.064, 2012.
- 11 Kim, Y., Knox, R. G., Longo, M., Medvigy, D., Hutya, L. R., Pyle, E. H., Wofsy, S. C.,
12 Bras, R. L., and Moorcroft, P. R.: Seasonal carbon dynamics and water fluxes in an
13 Amazon rainforest, *Global Change Biol.*, 18 (4), 1322–1334, doi: 10.1111/j.1365-
14 2486.2011.02629.x, 2012.
- 15 Laine, V., Venäläinen, A., Heikinheimo, M., and Hyvärinen, O.: Estimation of Surface Solar
16 Global Radiation from NOAA AVHRR Data in High Latitudes, *J. Appl. Meteorol.*, 38
17 (12), 1706–1719, doi:10.1175/1520-0450(1999)038<1706:EOSSGR>2.0.CO;2, 1999.
- 18 Lazzús, J. A., Pérez Ponce, A. A., and Marin, J.: Estimation of global solar radiation over the
19 city of La Serena (Chile) using a neural network, *Appl. Sol. Ener.*, 47 (1), 66–73, doi:
20 10.3103/S0003701X11010099, 2011.
- 21 Li, M.-F., Tang, X.-P., Wu, W., and Liu, H.-B.: General models for estimating daily global
22 solar radiation for different solar radiation zones in mainland China, *Energy Conv.*
23 *Manag.*, 70, 139–148, doi: 10.1016/j.enconman.2013.03.004, 2013.
- 24 Loew, A., Peng, J., and Borsche, M.: High-resolution land surface fluxes from satellite and
25 reanalysis data (HOLAPS~v1.0): evaluation and uncertainty assessment, *Geosci. Model*
26 *Dev.*, 9 (7), 2499–2532, doi:10.5194/gmd-9-2499-2016, 2016.
- 27 Lopez, G., and Batlles, F. J.: Estimating solar radiation from MODIS data, *Enrgy Proc.*, 49,
28 2362 - 2369, 2014, doi:10.1016/j.egypro.2014.03.250.
- 29 Malek, E.: Night-time evapotranspiration vs. daytime and 24h evapotranspiration, *J. Hydrol.*,
30 138(1), 119–129, doi:10.1016/0022-1694(92)90159-S, 1992.
- 31 Mallick, K., Jarvis, A., Wohlfahrt, G., Kiely, G., Hirano, T., Miyata, A., Yamamoto, S., and
32 Hoffmann, L.: Components of near-surface energy balance derived from satellite
33 soundings – Part 1: Noontime net available energy, *Biogeosciences*, 12, 433–451,
34 doi:10.5194/bg-12-433-2015, 2015.
- 35 Mauder, M., and Foken, T.: Impact of post-field data processing on eddy covariance flux
36 estimates and energy balance closure, *Meteorolog. Zeit.*, 15 (6), 597–609, doi:
37 10.1127/0941-2948/2006/0167 2006.

- 1 McCulloch, W. S., and Pitts, W.: A logical calculus of the ideas immanent in nervous activity,
2 The Bull. Math. Biophys., 5 (4), 115–133, doi: 10.1007/BF02478259, 1943.
- 3 Mubiru, J., and Banda, E. J. K. B.: Estimation of monthly average daily global solar
4 irradiation using artificial neural networks, Sol. Ener., 82 (2), 181–187, doi:
5 10.1016/j.solener.2007.06.003, 2008.
- 6 Parlange, M. B., and Katul, G. G.: Estimation of the diurnal variation of potential evaporation
7 from a wet bare soil surface, J. Hydrol., 132 (1-4), 71–89, doi: 10.1016/0022-
8 1694(92)90173-S, 1992.
- 9 Polo, J., Zarzalejo, L., and Ramírez, L.: Solar Radiation Derived from Satellite Images, In V.
10 Badescu (Ed.), Modeling Solar Radiation at the Earth's Surface SE - 18, 449–462,
11 Springer Berlin Heidelberg, doi: 10.1007/978-3-540-77455-6_18, 2008.
- 12 Ryu, Y., Baldocchi, D. D., Black, T. A., Detto, M., et al.: On the temporal upscaling of
13 evapotranspiration from instantaneous remote sensing measurements to 8-day mean
14 daily-sums, Agric. For. Meteorol., 152, 212–222, doi: 10.1016/j.agrformet.2011.09.010,
15 2012.
- 16 Senay, G. B., Velpuri, N. M., Bohms, S., Budde, M., et al.: Drought Monitoring and
17 Assessment: Remote Sensing and Modeling Approaches for the Famine Early Warning
18 Systems Network, In: Hydro-Meteorological Hazards, Risks, and Disasters, 233 - 262,
19 doi: 10.1016/B978-0-12-394846-5.00009-6, 2015.
- 20 Sepulcre-Canto, G., Vogt, J., Arboleda, A., and Antofie, T.: Assessment of the EUMETSAT
21 LSA-SAF evapotranspiration product for drought monitoring in Europe, Int. J. Appl.
22 Earth Obs. Geoinf., 30, 190–202, doi: 10.1016/j.jag.2014.01.021, 2014.
- 23 Shamshirband, S., Mohammadi, K., Tong, C. W., Zamani, M., et al.: A hybrid SVM-FFA
24 method for prediction of monthly mean global solar radiation, Theor. Appl. Climatol., 1–
25 13, doi: 10.1007/s00704-015-1482-2, 2015.
- 26 Shuttleworth, W. J., Gurney, R. J., Hsu, A. Y., and Ormsby, J. P.: FIFE: the variation in
27 energy partition at surface flux sites, IAHS Publ., 186, 67–74, 1989.
- 28 Tang, R., Li, Z.-L., and Sun, X.: Temporal upscaling of instantaneous evapotranspiration: An
29 intercomparison of four methods using eddy covariance measurements and MODIS data,
30 Remote Sens. Environ., 138, 102–118, doi: 10.1016/j.rse.2013.07.001, 2013.
- 31 Tang, R., Tang, B., Wu, H., Li, Z. L.: On the feasibility of temporally upscaling instantaneous
32 evapotranspiration using weather forecast information, Int. J. Remote Sens., 36 (19-20),
33 doi: 10.1080/01431161.2015.1029597, 2015.
- 34 Tolk, J. A., Howell, T. A., and Evett, S. R.: Nighttime evapotranspiration from alfalfa and
35 cotton in a semiarid climate, Agron. J., 98(3), 730 - 736, doi:10.2134/agronj2005.0276
36 2006.
- 37 Van Niel, T. G., McVicar, T. R., Roderick, M. L., van Dijk, A. I. J. M., et al.: Upscaling latent

1 heat flux for thermal remote sensing studies: Comparison of alternative approaches and
2 correction of bias, *J. Hydrol.*, 468–469, 35–46, doi: 10.1016/j.jhydrol.2012.08.005, 2012.

3 Wang, S.-C.: Artificial Neural Network. In: *Interdisciplinary Computing in Java*
4 *Programming SE - 5*, 743, 81–100, Springer US, doi: 10.1007/978-1-4615-0377-4_5,
5 2003.

6 Wang, D., Liang, S., He, T., Cao, Y., and Jiang, B.: Surface Shortwave Net Radiation
7 Estimation from FengYun-3 MERSI Data, *Remote Sens.*, 7, 6224-6239,
8 doi:10.3390/rs70506224, 2015

9 Wilson, K., Goldstein, A., Falge, E., Aubinet, M., et al.: Energy balance closure at FLUXNET
10 sites, *Agric. For. Meteorol.*, 113 (1–4), 223–243, doi: 10.1016/S0168-1923(02)00109-0,
11 2002.

12 Xu, T., Liu, S., Xu, L., Chen, Y., Jia, Z., Xu, Z., & Nielson, J.: Temporal Upscaling and
13 Reconstruction of Thermal Remotely Sensed Instantaneous Evapotranspiration, *Remote*
14 *Sens.*, 7 (3), 3400, doi: 10.3390/rs70303400, 2015.

15
16
17
18
19
20
21
22
23
24
25
26
27
28
29
30
31
32
33
34
35
36
37
38
39
40
41

1 **Table 1:** Statistical analysis of the performance of ANN in predicting R_{Sd} under varying sky
 2 conditions represented by four different classes of daily atmospheric transmissivity (τ). Here the
 3 statistical metrics of R_{Sd_pred} for two different upscaling hours (1100 and 1330 h) are presented.

Time-of-day (h)	τ	R^2	RMSE ($MJ\ m^{-2}\ d^{-1}$)	IA	MAPE	Bias ($MJ\ m^{-2}\ d^{-1}$)
1100	τ_1	0.67	1.84	0.67	53.56	1.12
	τ_2	0.79	2.45	0.80	16.69	0.59
	τ_3	0.88	2.30	0.82	9.17	-0.74
	τ_4	0.98	0.63	0.95	1.69	0.08
1330	τ_1	0.65	1.77	0.67	51.50	1.06
	τ_2	0.81	2.44	0.81	16.83	0.69
	τ_3	0.89	2.23	0.83	8.94	-0.85
	τ_4	0.98	0.89	0.95	2.40	-0.46

4
 5
 6
 7
 8
 9
 10
 11
 12

1 **Table 2:** A summary of ET_d error statistics by comparing the performance of R_S -based, $R_S TOA$ -based and EF -based ET_i
 2 upscaling methods with regard to different sky conditions. Here τ_1 represents low atmospheric transmissivity due to high
 3 cloudiness while τ_4 represents high transmissivity under clear sky conditions.

Time-of-day (h)	τ	R^2			RMSE ($\text{MJ m}^{-2} \text{d}^{-1}$)			IA			MAPE			Bias ($\text{MJ m}^{-2} \text{d}^{-1}$)		
		R_S	$R_S TOA$	EF	R_S	$R_S TOA$	EF	R_S	$R_S TOA$	EF	R_S	$R_S TOA$	EF	R_S	$R_S TOA$	EF
1100	τ_1	0.49	0.32	0.32	1.34	1.65	2.07	0.72	0.67	0.71	50.14	66.70	64.19	-0.13	-0.04	0.05
	τ_2	0.72	0.70	0.69	1.73	1.81	1.93	0.81	0.78	0.69	26.47	32.41	36.42	-0.21	-0.19	-0.95
	τ_3	0.72	0.73	0.79	1.99	1.94	2.38	0.81	0.79	0.59	24.69	25.66	40.37	-0.24	-0.37	-1.78
	τ_4	0.77	0.81	0.68	1.32	1.13	2.00	0.84	0.81	0.49	32.17	30.02	55.43	0.05	-0.19	-1.34
1330	τ_1	0.52	0.34	0.29	1.21	1.68	2.34	0.73	0.69	0.71	48.29	66.09	68.14	-0.11	0.08	0.12
	τ_2	0.73	0.72	0.71	1.71	1.93	1.86	0.82	0.79	0.71	26.12	33.71	35.33	-0.01	0.24	-0.88
	τ_3	0.75	0.75	0.76	1.89	1.96	2.43	0.82	0.82	0.61	23.17	25.82	41.65	0.09	0.14	-1.75
	τ_4	0.79	0.86	0.80	1.32	1.09	1.86	0.84	0.86	0.49	29.54	26.59	53.91	0.10	0.11	-1.38

4
5
6
7
8
9
10
11
12

1 **Table 3:** Error statistics of ET_{d_pred} at four different temporal scales from three ET_i upscaling methods.

Time-of-day (h)	Temporal scale	R^2			RMSE ($\text{MJ m}^{-2} \text{d}^{-1}$)			IA			MAPE			Bias ($\text{MJ m}^{-2} \text{d}^{-1}$)		
		R_S	$R_{S\text{TOA}}$	EF	R_S	$R_{S\text{TOA}}$	EF	R_S	$R_{S\text{TOA}}$	EF	R_S	$R_{S\text{TOA}}$	EF	R_S	$R_{S\text{TOA}}$	EF
1100	Daily	0.71	0.72	0.71	1.79	1.85	2.16	0.82	0.80	0.67	28.80	32.98	57.00	0.19	0.22	1.21
	8-days	0.86	0.84	0.85	1.17	1.22	1.65	0.87	0.86	0.67	18.50	20.63	46.96	0.19	0.22	1.16
	Monthly	0.89	0.88	0.88	0.99	1.04	1.61	0.89	0.67	0.67	15.52	17.22	49.72	0.19	0.22	1.16
	Annually	0.92	0.91	0.93	0.57	0.62	1.33	0.87	0.84	0.54	11.12	12.54	45.88	0.19	0.22	1.21
1330	Daily	0.75	0.74	0.69	1.74	1.89	2.2	0.83	0.82	0.67	26.59	29.89	56.45	-0.04	0.17	-1.18
	8-days	0.87	0.86	0.84	1.11	1.21	1.7	0.88	0.88	0.68	16.80	17.97	50.36	-0.04	0.17	-1.18
	Monthly	0.90	0.90	0.87	0.93	1.00	1.59	0.90	0.89	0.68	13.69	14.85	48.08	-0.04	0.17	-1.18
	Annually	0.93	0.93	0.92	0.51	0.53	1.31	0.88	0.88	0.54	9.00	9.70	44.13	-0.04	0.17	-1.18

2
3
4
5
6
7
8
9

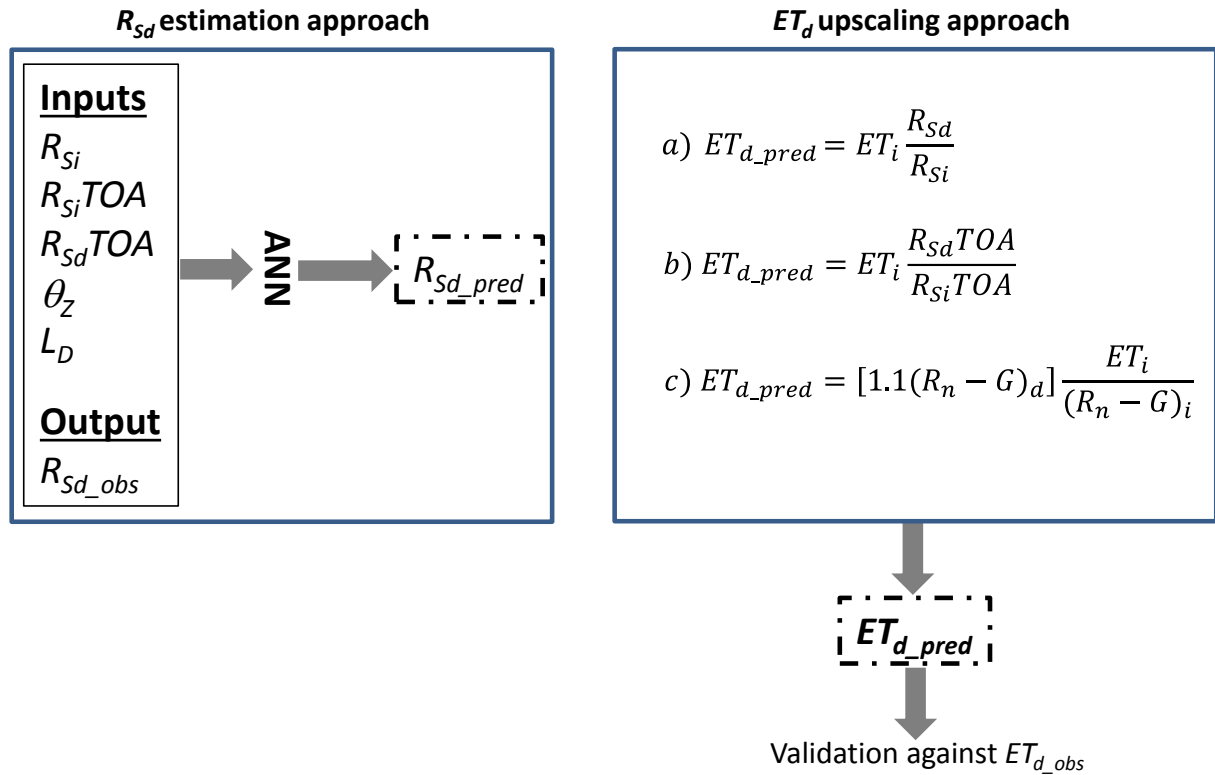
1 **Table 4:** Evaluation of the R_g -based ANN predicted ET_d (ET_{d_pred}) error statistics based on ‘closed’ (EBC) and unclosed’ (EBO) surface energy balance
2 under varying sky conditions represented by four different classes of daily atmospheric transmissivity (τ). Here τ_1 represents low atmospheric
3 transmissivity due to high cloudiness while τ_4 represents high transmissivity under clear sky conditions. The statistical metrics of ET_{d_pred} for two
4 different upscaling hours (1100 and 1330 h) are presented.

Time-of-day (h)	τ	R^2		RMSE (MJ m ⁻² d ⁻¹)		IA		MAPE		Bias (MJ m ⁻² d ⁻¹)	
		EBO	EBC	EBO	EBC	EBO	EBC	EBO	EBC	EBO	EBC
1100	τ_1	0.37	0.17	2.96	3.31	0.71	0.57	87.21	86.49	0.66	1.12
	τ_2	0.68	0.54	1.64	2.94	0.78	0.68	28.66	38.01	-0.10	0.65
	τ_3	0.75	0.61	1.77	3.20	0.76	0.66	25.31	37.82	-0.67	1.34
	τ_4	0.66	0.61	1.09	3.40	0.71	0.30	21.77	85.80	-0.31	3.83
1330	τ_1	0.35	0.25	2.02	2.70	0.71	0.60	69.78	78.18	0.37	0.87
	τ_2	0.76	0.5	1.54	3.27	0.81	0.69	27.56	40.98	0.23	0.63
	τ_3	0.77	0.59	1.66	3.18	0.80	0.70	23.16	34.17	-0.46	0.76
	τ_4	0.84	0.64	0.98	2.46	0.76	0.66	23.30	43.89	-0.56	1.23

5

6

Figure 1. A conceptual diagram of the methodology. On the left side is a representation of predicting daily incoming short wave radiation (R_{Sd_pred}). The ANN is trained to learn the system response to a combination of explanatory variables i.e. instantaneous incoming short wave radiation (R_{Si}), instantaneous exo-atmospheric shortwave radiation ($R_{Si}TOA$), daily exo-atmospheric shortwave radiation ($R_{Sd}TOA$), solar zenith angle (θ_z), and day length (L_D), by being fed with a sample data of observed daily incoming short wave radiation (R_{Sd_obs}) which is the dependant variable. On the right side are methods of upscaling instantaneous (ET_i) to daily ET (ET_d) using our R_S -based method (a) and other two approaches (b, c) are the R_{STOA} and EF -based methods respectively used which are used for comparison.



2

3

4

5

6

7

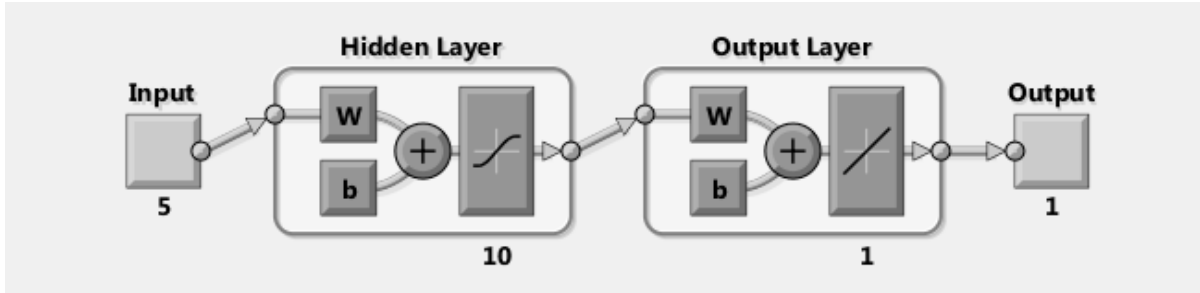
8

9

10

1

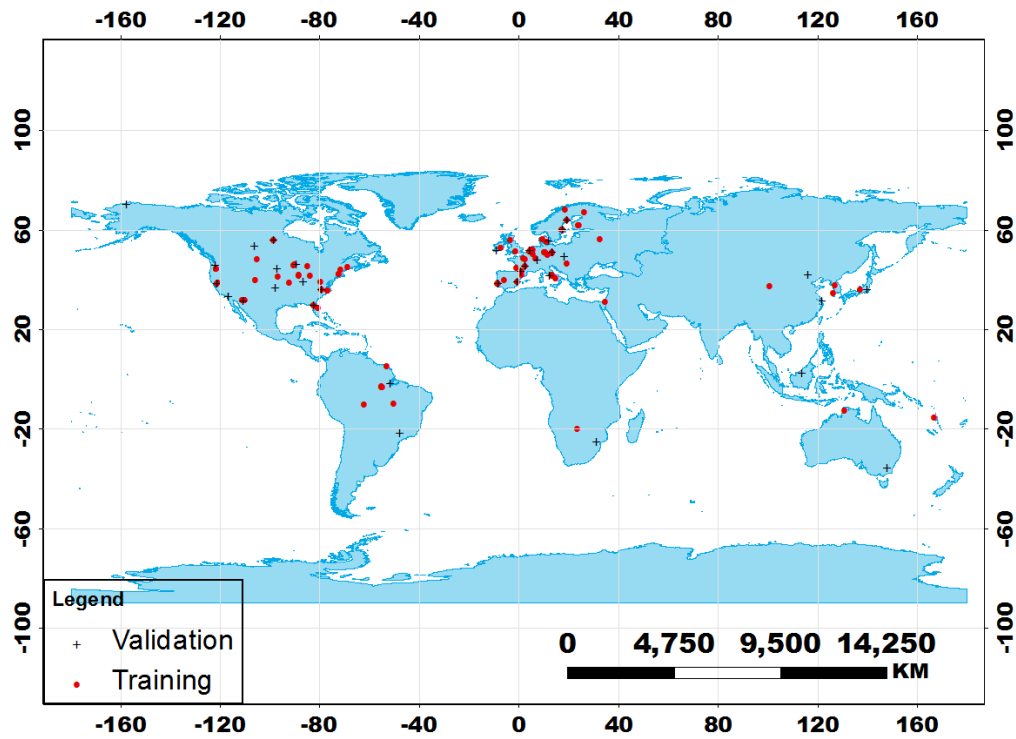
Figure 2. Schematic representation of a simple artificial network model. The artificial neuron has five input variables, for the intended output. These inputs are then assigned weights (W) and bias (b), and the sum of all these products (Σ) is fed to an activation function (f). The activation function alters the signal accordingly and passes the signal to the next neuron(s) until the output of the model is reached (Mathworks, 2015).



2

1

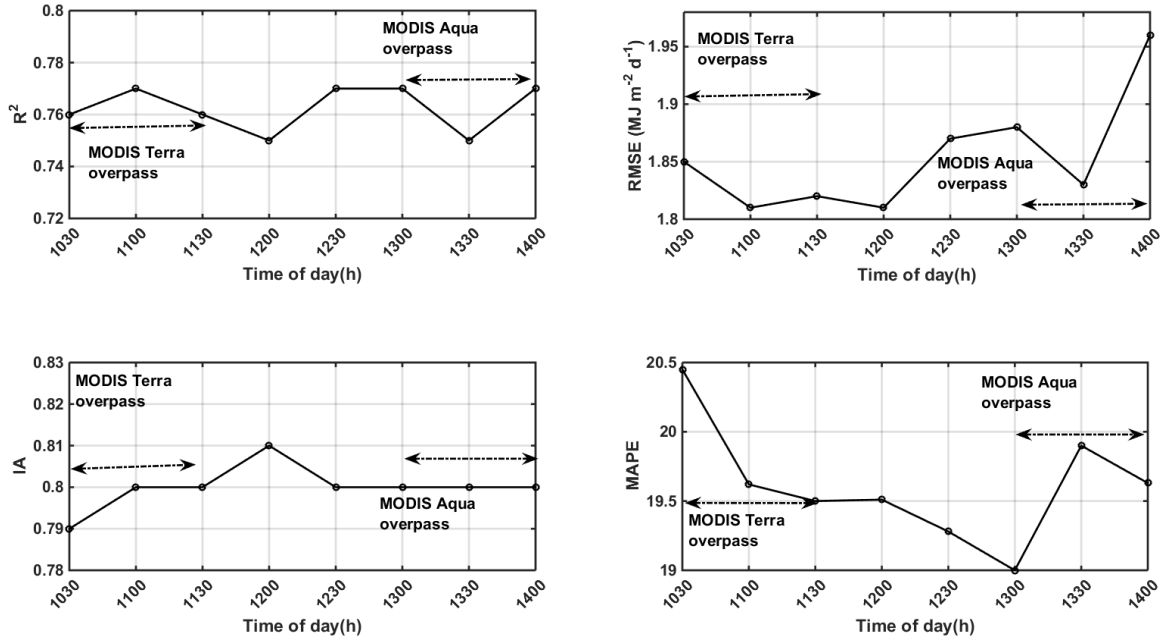
Figure 3. Distribution of 126 sites of the FLUXNET eddy covariance network used in the present study with 85 and 41 sites for training and validation, respectively between the years 1999 and 2006.



2
3
4
5
6
7
8
9
10
11
12
13
14
15

1

Figure 4. Statistical metric of R_{Sd_pred} by ANN for different time-of-day. As the study is intended for remote sensing application, we demonstrate the potential of the method for future research in the case where satellite will be used and as such we pick MODIS overpass time as an example to highlight on the predictive ability of the ANN at the specific overpass times.



2

3

4

5

6

7

8

9

10

11

12

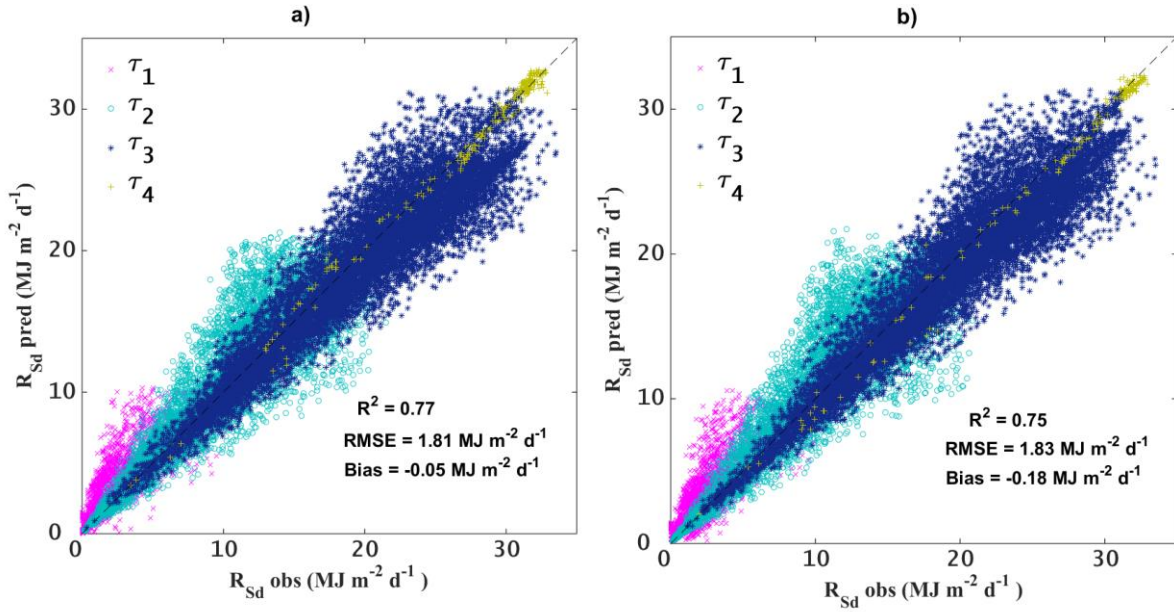
13

14

15

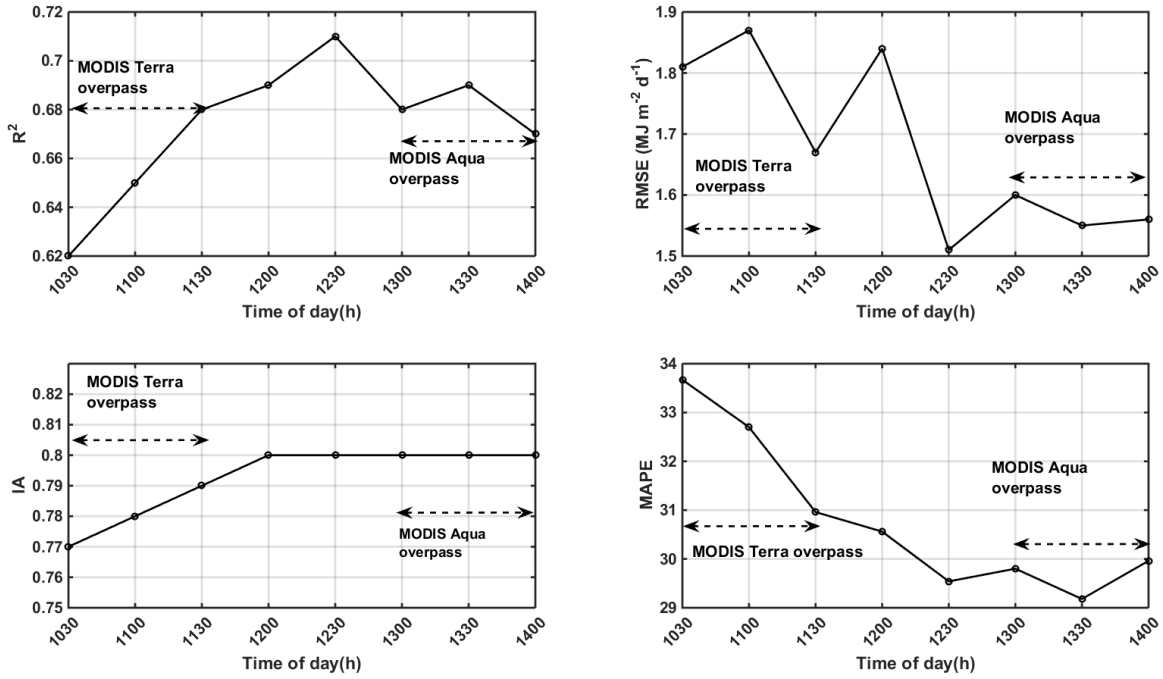
1

Figure 5. Scatter plots between R_{Sd_obs} versus R_{Sd_pred} for different levels of daily atmospheric transmissivity classes (τ) from (a) 1100 and (b) 1330 hours upscaling. Here τ_1 – τ_4 represent daily atmospheric transmissivity of four different class, $0.25 \geq \tau \geq 0$, $0.50 \geq \tau \geq 0.25$, $0.75 \geq \tau \geq 0.50$, and $1 \geq \tau \geq 0.75$, respectively, with τ_1 signifying high degree of cloudiness (or overcast skies) whereas τ_4 indicates clear skies.



2
3
4
5
6
7
8
9
10
11
12
13
14
15

Figure 6. Statistical summary of ET_{d_pred} for different time-of-day using Eq. (1) based on R_{Si} and R_{Sd_pred} . As the study is intended for remote sensing application, we once again demonstrate the potential of the method for future research in the case where satellite will be used and as such we pick MODIS Terra-Aqua overpass time.



2

3

4

5

6

7

8

9

10

11

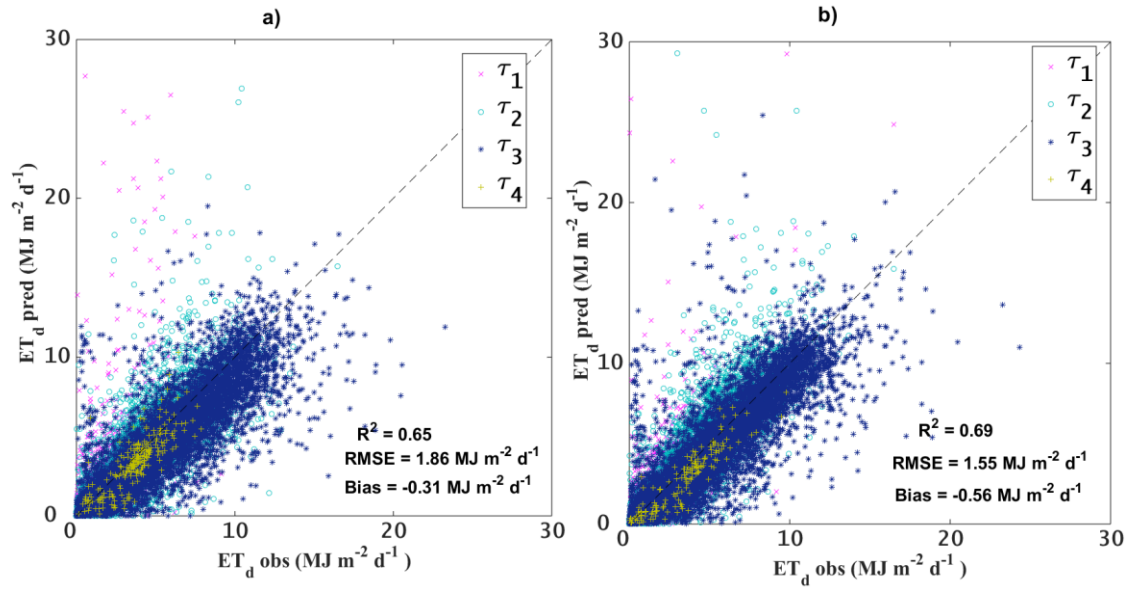
12

13

14

1

Figure 7. ET_{d_pred} obtained through eq. (1) versus ET_{d_obs} for different levels of τ from both forenoon (a) and afternoon (b) upscaling (1100 and 1300 h daytime hours).



2

3

4

5

6

7

8

9

10

11

12

13

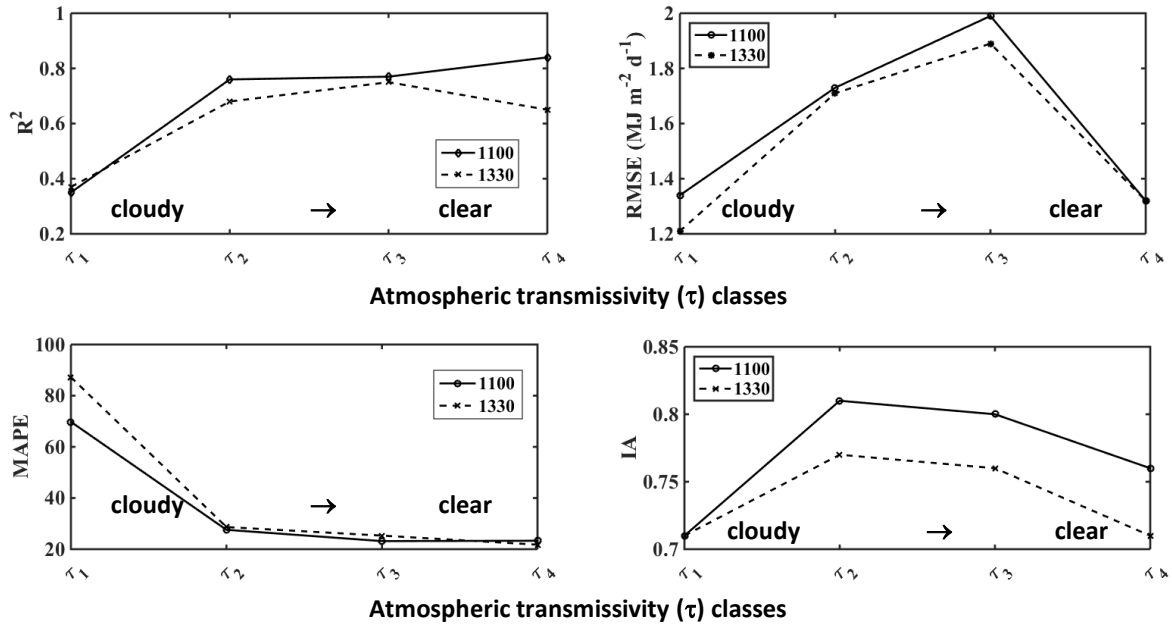
14

15

16

17

Figure 8. Assessing the statistical metrics of $ET_{d,pred}$ (using eq.1) for different levels of daily atmospheric transmissivity classes (representing cloudy to clear skies) for both 1100h and 1330h time-of-day ET_i scaling.



2

3

4

5

6

7

8

9

10

11

12

13

14

15

16

Figure 9. An intercomparison of ET_{d_pred} error statistics (RMSE and MAPE) for different levels of atmospheric transmissivity classes based on two different ANN training (ANN trained with shortwave radiation and astronomical variables only; and ANN trained with radiation, astronomical variables, soil moisture and rainfall) based on 1100h and 1330h time-of-day ET_i scaling.

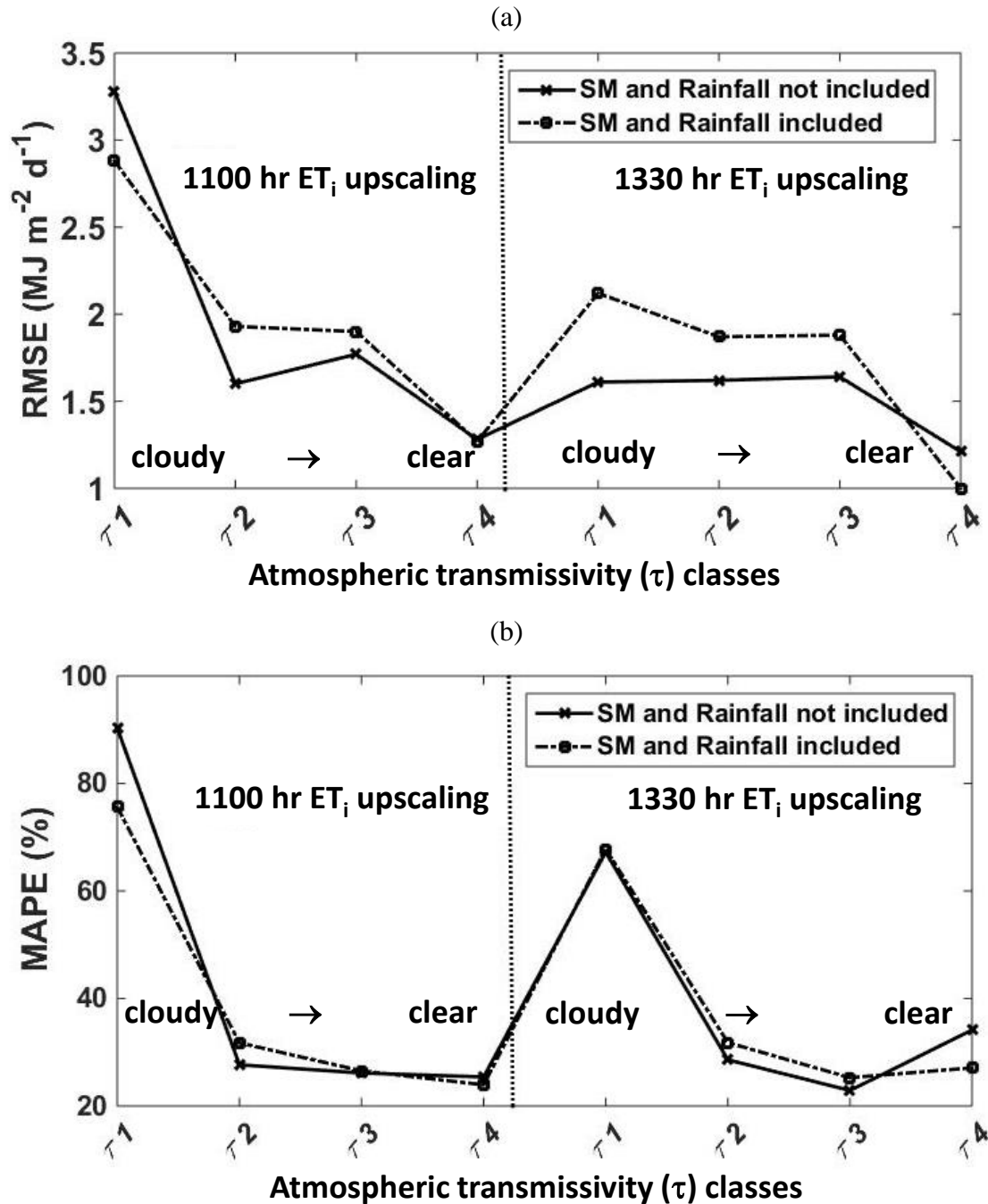


Figure 10. Time series comparison between observed and predicted ET_d for four representative sites located in Australia, Brazil, South Africa and Sweden.

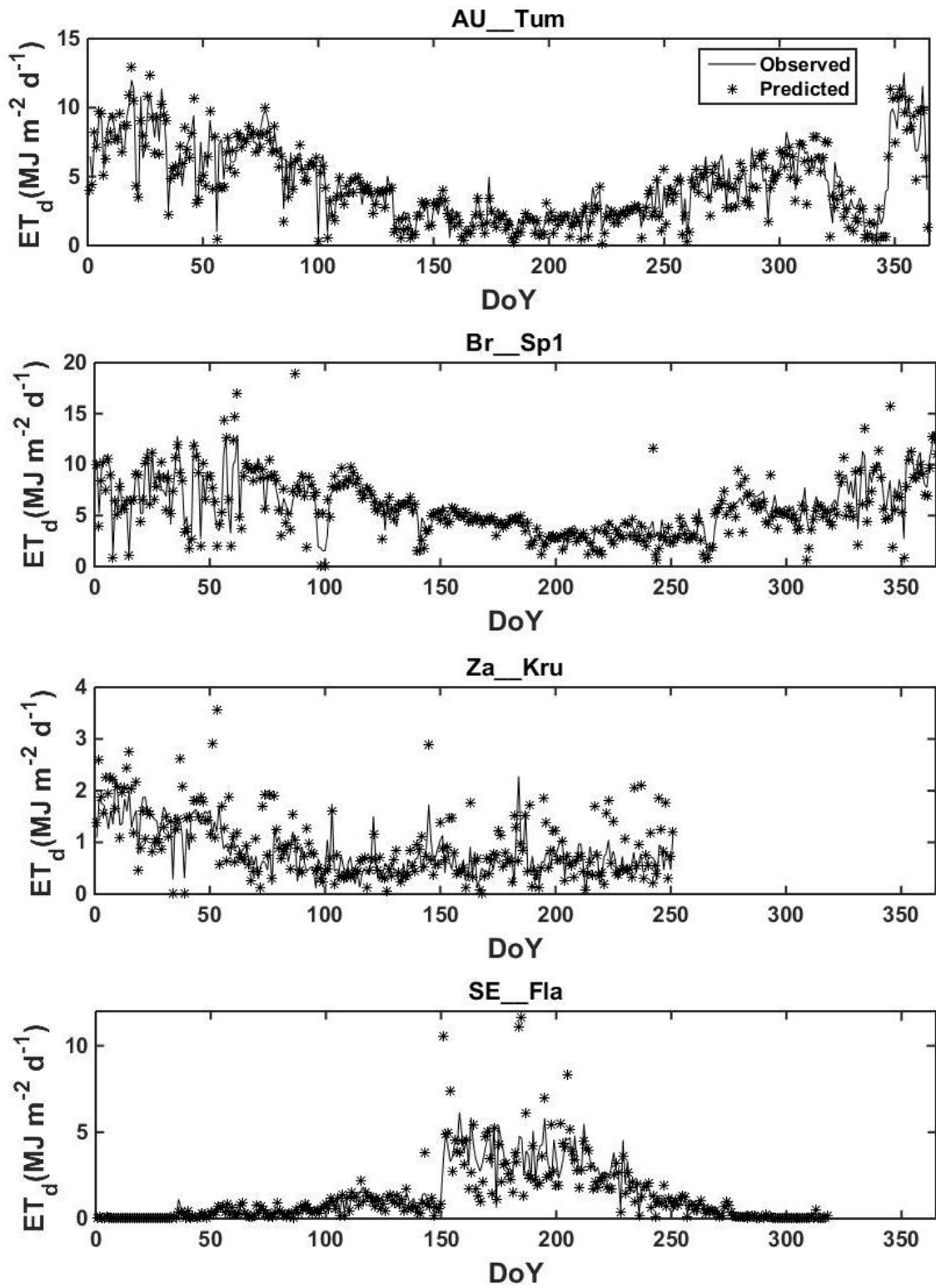
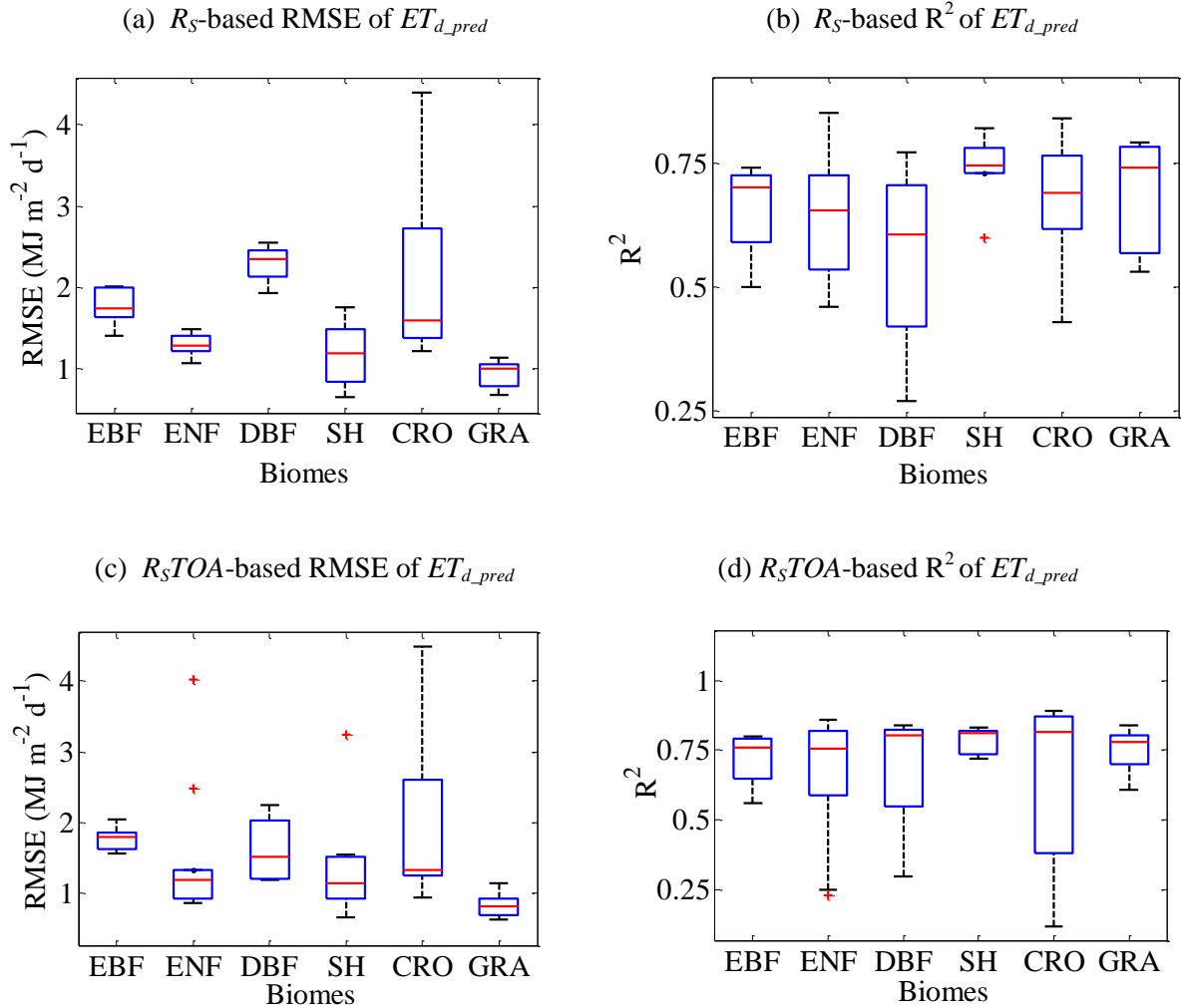


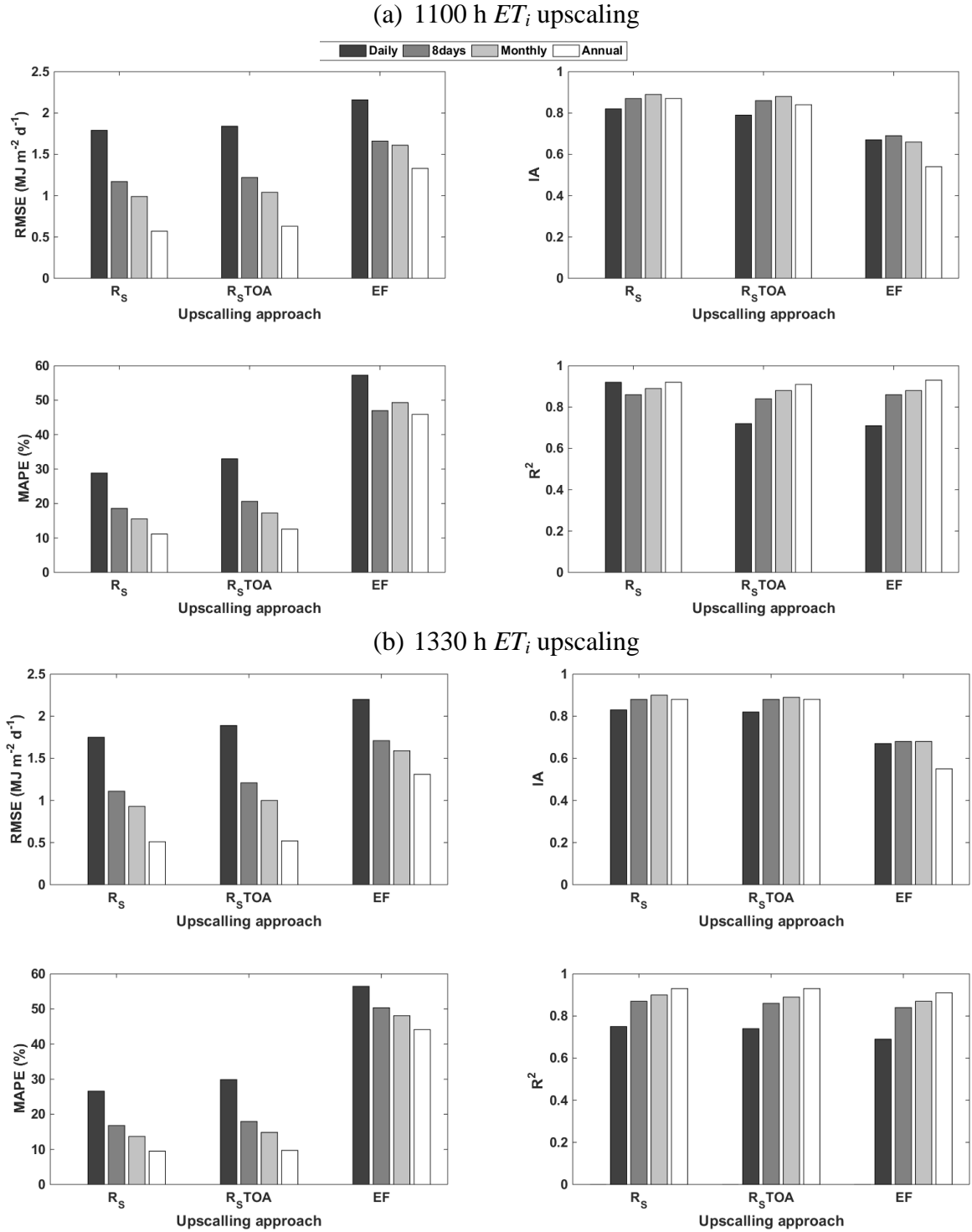
Figure 11. Biome specific error characteristics of ET_{d_pred} displaying the box plots of RMSE and coefficient of determination (R^2) from both R_S -based and $R_{S_{TOA}}$ -based ET_i upscaling. The biome classes are evergreen broadleaf forest (EBF), evergreen needleleaf forest (ENF), deciduous broadleaf forest (DBF), shrubland (SH), cropland (CRO), and grassland (GRA), respectively.



2
3
4
5
6
7
8
9
10
11
12

1

Figure 12. Statistical metrics of $ET_{d,pred}$ from three different ET_i upscaling approaches [shortwave incoming radiation (R_s), exo-atmospheric shortwave radiation (R_{sTOA}) and evaporative fraction (EF)] at different temporal scales based on ET_i measurements at (a) 1100h and (b) 1330h time-of-day.

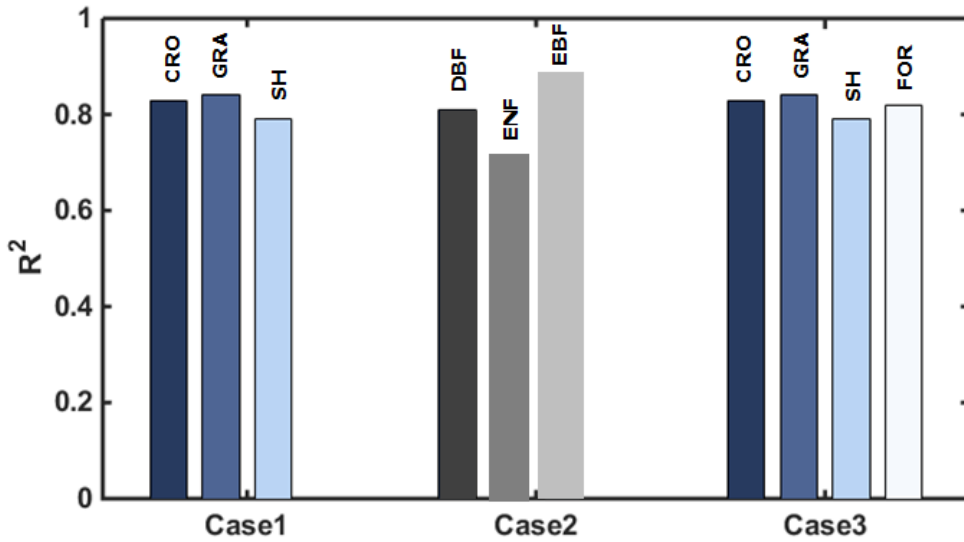


2
3

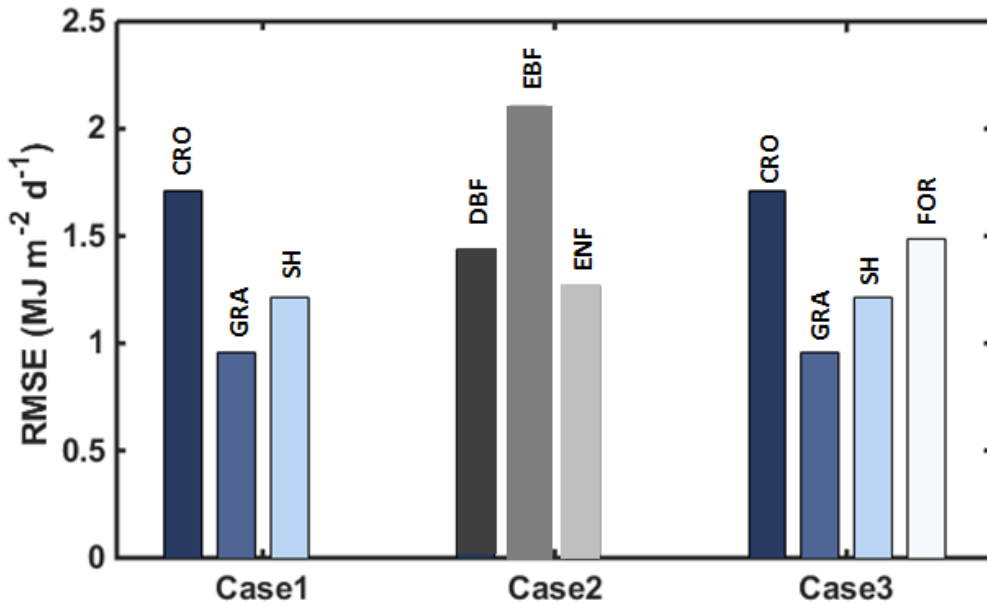
1

Figure 13. Illustrative examples of the sensitivity of ET_{d_pred} error statistics (R^2 and RMSE) to the different biome type scenarios of ANN training. Here, Case1 consist of training the ANN with forest (FOR) datasets and evaluating ANN predicted ET_d statistics on non-forest biomes, Case2 consist of training the ANN with non-forest datasets and evaluating ANN predicted ET_d statistics on forest biomes, Case3 consist of training the ANN with both forests and non-forest datasets and evaluating ANN predicted ET_d statistics on all the biomes.

(a) R^2 of ET_{d_pred} for three different ANN training scenarios



(b) RMSE of ET_{d_pred} for three different ANN training scenarios



2